AFRL-AFOSR-UK-TR-2023-0066

Microstructure and damage evaluation for fibre-reinforced composites

Patterson, Eann A.
THE UNIVERSITY OF LIVERPOOL
BROWNLOW HILL
LIVERPOOL, , L69 7ZX
GBR

06/30/2023
Final Technical Report

Air Force Research Laboratory
Air Force Office of Scientific Research
European Office of Aerospace Research and Development
Unit 4515 Box 14, APO AE 09421

REPORT DOCUMENTATION PAGE

PLEASE DO NOT RETURN YOUR FORM TO THE ABOVE ORGANIZATION.

1. REPORT DATE
20230630

2. REPORT TYPE
Final

3. DATES COVERED

START DATE 20200928	**END DATE** 20230331

4. TITLE AND SUBTITLE
Microstructure and damage evaluation for fibre-reinforced composites

5a. CONTRACT NUMBER	**5b. GRANT NUMBER** FA8655-20-1-7034	**5c. PROGRAM ELEMENT NUMBER**
5d. PROJECT NUMBER	**5e. TASK NUMBER**	**5f. WORK UNIT NUMBER**

6. AUTHOR(S)
Eann A. Patterson

7. PERFORMING ORGANIZATION NAME(S) AND ADDRESS(ES)
THE UNIVERSITY OF LIVERPOOL
BROWNLOW HILL
LIVERPOOL L69 7ZX
GBR

8. PERFORMING ORGANIZATION REPORT NUMBER

9. SPONSORING/MONITORING AGENCY NAME(S) AND ADDRESS(ES)
EOARD
UNIT 4515
APO AE 09421-4515

10. SPONSOR/MONITOR'S ACRONYM(S)
AFRL/AFOSR IOE

11. SPONSOR/MONITOR'S REPORT NUMBER(S)
AFRL-AFOSR-UK-TR-2023-0066

12. DISTRIBUTION/AVAILABILITY STATEMENT
A Distribution Unlimited: PB Public Release

13. SUPPLEMENTARY NOTES

14. ABSTRACT
The research programme had three objectives, namely: (a) to develop an approach to quantify the relationship between microstructural features such as void morphology (shape and orientation), matrix rich zones and local fibre angle; (b) to apply orthogonal decomposition to volumes (tensors) of measurements to characterise three-dimensional microstructures based on computed tomography data; and (c) to explore the effects of loading rate on the development of damage using strain-based measurements described by feature vectors. The impact of the pandemic severely constrained the progress of research in a laboratory environment and the recruitment of new research personnel during 2021 and was alleviated by a no-cost extension. Good progress has been made against all objectives and the research programme has been completed on schedule.

15. SUBJECT TERMS

16. SECURITY CLASSIFICATION OF:

a. REPORT U	**b. ABSTRACT** U	**c. THIS PAGE** U

17. LIMITATION OF ABSTRACT
SAR

18. NUMBER OF PAGES
41

19a. NAME OF RESPONSIBLE PERSON
DAVID SWANSON

19b. PHONE NUMBER *(Include area code)*
785-6565

Standard Form 298 (Rev.5/2020)
Prescribed by ANSI Std. Z39.18

Microstructure and damage evaluation for fibre-reinforced composites

Final Report	
Submitted	8th June 2023
Grant No:	FA8655-20-1-7034
Period of Performance:	28 September 2020 to 31 March 2023
Period of Grant:	28 September 2020 to 31 March 2023
Principal Investigator:	Prof Eann Patterson, University of Liverpool
Co-Principal Investigator:	Dr Will Christian, University of Liverpool
Report co-author:	Dr Ceri Middleton, University of Liverpool
Collaborator:	Dr Craig Przybyla, USAF AFMC AFRL/RXCCP
Program Manager:	Maj. David D. Swanson, USAF EOARD

SUMMARY

The research programme had three objectives, namely: (a) to develop an approach to quantify the relationship between microstructural features such as void morphology (shape and orientation), matrix rich zones and local fibre angle; (b) to apply orthogonal decomposition to volumes (tensors) of measurements to characterise three-dimensional microstructures based on computed tomography data; and (c) to explore the effects of loading rate on the development of damage using strain-based measurements described by feature vectors. The impact of the pandemic severely constrained the progress of research in a laboratory environment and the recruitment of new research personnel during 2021, and was alleviated by a no-cost extension. Good progress has been made against all objectives and the research programme has been completed on the revised schedule.

Please direct any questions regarding the content of this report to Eann Patterson (eann.patterson@liverpool.ac.uk)

CONTENTS

ACCOMPLISHMENTS

- Research Objectives:
    - To develop an approach to quantifying the relationship between microstructural features such as void morphology (shape and orientation), matrix-rich zones and local fibre angle;
    - To apply orthogonal decomposition to volumes (tensors) of measurements to characterise three-dimensional microstructures based on computed tomography data; and
    - To explore the effects of loading rates on the development of damage using strain-based measurements described by feature vectors.

- Accomplishments during the project.
    - Progress has been made against all three objectives.
    - Volume decomposition has been used to extract information about the shape of microstructural features observed in serial micrographs provided by AFRL. It has been demonstrated that the feature vectors obtained from the decomposition process characterise the morphology of the microstructure and this approach has the potential to be used to establish relationships between fibres, void and matrix rich zones.
    - Volume decomposition has been used to identify damage locations in tomography data, provided by AFRL, at two different length scales: individual fibres and within the bulk volume. Indications of damage are given by high differences between the feature vectors, which correlate to visually observable damage at both length scales.
    - Impact tests have been performed on composite panels manufactured at the university. Surface displacements and strains were obtained using a high-speed digital image correlation system and feature vectors were subsequently extracted that describe the displacement field as a function of time. These feature vectors can be used to characterise the damage caused by the impact.

- How were the results disseminated to communities of interest? If there is nothing significant to report during this reporting period, state "Nothing to Report."
    - Emami-Tabrizi I, Christian WJR, Przybyla C, Patterson EA. (2023) 'Comparing 3D Matrix Rich Zones in Ceramic Matrix Composites Using Orthogonal Decomposition'. To be presented at the 17th International Conference on Advances in Experimental Mechanics (Aug-Sept, 2023).
    - Middleton CA, Amjad, K, Christian WJR, Przybyla C, Patterson EA 'Detecting damage in mini-composite specimens using volume decomposition'. In

    preparation, for submission to IEEE, summer 2023.
  - Christian WJR, Lambert P, Emami-Tabrizi I, Middleton CA, Przybyla C, Patterson EA ‘Measuring the morphology of fatigue damage in composite components during fatigue tests’. In preparation.

- (Interim Reports Only) What do you plan to do during the next reporting period to accomplish the goals and objectives? If there are no changes to the agency-approved application or plan for this project or if this is the final report, state “Nothing to Report.”
  - Final report: therefore nothing to report.

IMPACTS

Development of the principal discipline(s) of the project

The advances in and demonstration of the volume decomposition technique are likely to have an impact across the discipline because the technique both reduces the dimensionality of volumes of data, which allows more straightforward statistical comparisons to be made, and enables the identification of shapes and trends in the data. This is likely to stimulate a shift from largely subjective comparisons of data to objective, quantifiable comparisons of datasets from different experiments or from models and experiments.

Other disciplines:

The techniques for comparing the characteristics of large volumes of data and distinguishing differences between the characteristics of datasets is likely to have wide ranging applications. Earlier work on characterising uncertainties in large datasets has found applications in both engineering and environmental sciences, see for example Alexiadis et al, 2021 [1].

Describe the impact in this reporting period on the development of human resources

A post-doctoral researcher has been trained in the use of decomposition techniques for comparing datasets. The research team has supervised two Masters projects in which data comparison techniques have been utilised.

Describe the impact on teaching and educational experiences

No new materials have been developed.

Describe the impact in this reporting period on physical, institutional, and information resources that form infrastructure.

The impact test rig in the investigators' laboratory has been recommissioned and upgraded to support the activity under objective (c) above.

Impact on society beyond science and technology:

The principal investigator (PI) delivered two Pint of Science talks during festivals targeted at the general public in 2022 and 2023 [https://pintofscience.co.uk/]. The PI also writes a weekly blog [https://realizeengineering.blog/], which is read in more than 150 countries, and has featured data decomposition relevant to the work in this project on a number of occasions.

CHANGES

Changes in approach - none

Problems or delays - none

Expenditure Impacts - none

Significant changes in the use or care of human subjects, vertebrate animals and/or biohazards

Not applicable.

Changes to the primary place of performance from that originally proposed - none.

TECHNICAL UPDATE

1. Introduction

This report describes work performed at the University of Liverpool in collaboration with colleagues at AFRL. It covers a research programme which ran from September 2020 to March 2023.

The sheer size and complexity of data related to the heterogenous microstructure of composite materials can obstruct our understanding of their processing-structure-properties relationship. Moreover, the necessity for utilizing materials at extreme conditions has amplified the requirement for proper analysis of microstructures. Ceramic matrix composites (CMC) with low density, high specific strength/modulus, and oxidative resistance are being introduced as a reliable material for hypersonic regime engines and propulsion systems [2-5]. However, the brittle behaviour of these composites arising from processing defects complicates their application. Microstructural imperfections such as voids can be detrimental to performance of CMCs and it is crucial to increase the degree of densification for CMCs to prolong their service life. Over the previous couple of decades, advancements in manufacturing techniques and material modifications have resolved this issue to some extent [6-8], while the major issue of characterizing large microstructural datasets in composites using a rigorous method has received less attention than other aspects [9-11]. Most experimental studies on microstructural characterization of ceramic matrix composites have been focused on the interpretation of 2D data, which might result in misleading conclusions about material properties. Using 3D data to characterize the heterogeneous structure of composites in general can be more reliable despite resulting in even larger datasets.

Recently, image processing techniques have been used to extract 3D images of voids inside a SiC_f/SiNC composite. This was applied to a sizable dataset consisting of microscope images obtained via serial sectioning provided by AFRL [12]. The dimensionality of the volumetric data was reduced using 2D orthogonal decomposition to obtain feature vectors that described each of the voids. These feature vectors were then used to characterise the shapes of the voids. In parallel to this work, digital image correlation was used to identify the fibre orientation fields based on micrograph images of the same dataset. The 3D structure of voids and fibres represented by orientation maps were combined and the relationship between laminar angles and void shape descriptors were presented. 2D orthogonal decomposition using Chebyshev orthogonal polynomials significantly reduces the dimensionality of data without loss of the important characteristics and its richness [13]. The extension of the 2D orthogonal decomposition technique into 3D spatial data has been used for FEM model validation via comparison with digital volume correlation data provided by AFRL [14]. It was shown that feature vectors obtained via volume decomposition enabled data compression ratios up to 32000:1, with reconstruction errors within the uncertainty range of the experimental data.

The demonstrated capability of volume decomposition in reducing dimensionality, and AFRL's ability to obtain large datasets from serial sectioning and X-ray computed tomography triggered further investigation of these data sets using 3D orthogonal decomposition in the current project. In addition to this, methods of characterising the propagation of damage in loaded composite samples [15], which was explored in the previous project, serve as a starting point for a new study employing volume decomposition to analyse high strain rate damage events.

Accordingly, the following objectives were defined for the current project to expand the application of orthogonal decomposition in analysis of large experimental datasets of composite materials:

a. To develop an approach to quantifying the relationship between microstructural features such as void morphology (shape and orientation), matrix-rich zones and local fibre angle;
b. To apply orthogonal decomposition to volumes (tensors) of measurements to characterise three-dimensional microstructures based on computed tomography data; and
c. To explore the effects of loading rates on the development of damage using strain-based measurements described by feature vectors.

These objectives have been achieved and the resultant research is described in the following sections.

2. An approach to quantifying the relationship between microstructural features

The section describes the research performed to achieve objective (a) to develop an approach to quantifying the relationship between microstructural features such as void morphology (shape and orientation), matrix-rich zones and local fibre angle.

2.1 Raw data and pre-processing of images

The raw data consisted of 100 microscope mosaics of a SiC_f/SiNC ceramic matrix composite obtained via serial sectioning technique which was supplied by AFRL. The section micrographs, consisting of 6930×4800 pixels, were created by stitching 36 microscope images together. The depth difference between the consecutive micrographs was 1 µm and the spatial resolution was 0.522 µm/pixel. A sample micrograph is shown in Figure 2-1.

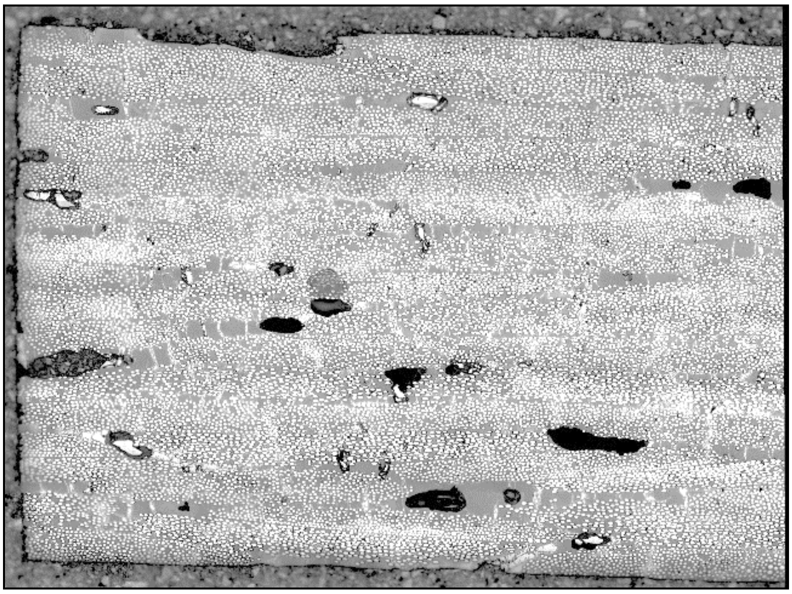

Figure 2-1 A sample micrograph with size of 2358 µm × 2860 µm

2.2 Image processing and feature extraction

Image processing of the raw data was performed with two goals. These were to minimize the misalignment between the sequential sections, and to extract 2D areas related to fibres, void defects and matrix rich zones using image segmentation. To complete the image processing steps, all micrographs are imported into a suite of specially-written MATLAB algorithms. Since small translational movements of the sample during the sectioning sequence could result in serrated surfaces on extracted volumetric objects, each image in the sequence was aligned with respect to its predecessor using an intensity-based image registration technique [16]. This method is easily implemented using a predefined function wherein translation, rotation, scale, and shear transformations are performed using an optimized similarity metric. Image registration aligned the target image with respect to a reference image and ensured that they are in the same coordinate system.

Since the intensity level of voids, matrix and fibres are different in a micrograph, grayscale thresholding was used to segment the image. An approach consisting of thresholding based on Otsu’s method and morphological operations, as used and reported previously, was used to identify the low intensity voids in the images [12]. However, for the extraction of the fibres and matrix phases a slightly different approach was performed as described below.

2.3 Segmentation of the fibres

As seen in the intensity histogram in Figure 2-2, the fibre phase is readily separable from the other phases due to its higher grey values by using Otsu's thresholding. However, using Otsu's thresholding method to separate fibres and binarizing the image results in inclusion of some high intensity matrix phase adjacent to void defects and shrinkage cracks as seen in Figure 2-3 (top). These high intensity regions have elongated or noncircular shapes. To remove these ill-sorted high intensity regions, morphological opening was performed on the binary image followed by erosion to remove small areas of noise and to disconnect objects joined by fine lines. The resulting binary image consisted of separate circular white regions which indicated cross section of the fibres, and few non-circular high intensity areas related to the matrix. Thus, each white region (object) in the binary data could be easily labelled and characterized based on its centroid coordinates, major axis length, minor axis length, spatial orientation and area. This procedure was accomplished using the "bwconncomp" function available in MATLAB. After characterizing distinct high intensity regions, two parameters were used to distinguish circular objects from noncircular ones.

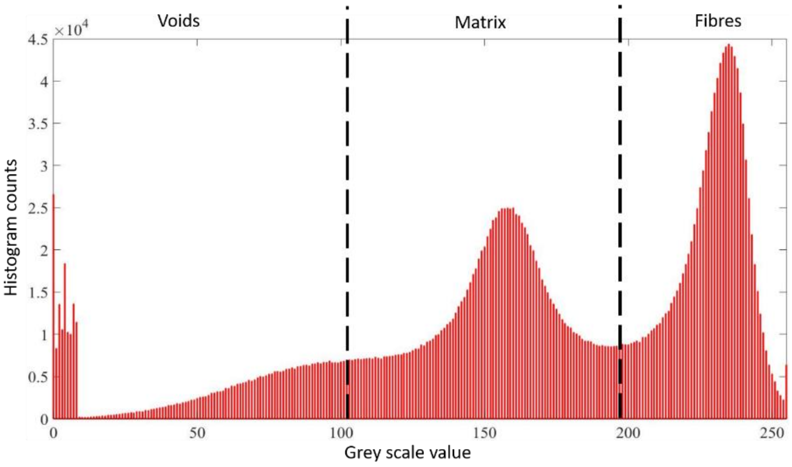

Figure 2-2 Typical histogram of greyscale intensities for the microscope images

To remove the non-circular areas in the binary image, the roundness of each individual object was obtained by calculating the ratio of "4 × π × area of the object" to the square of its perimeter. This ratio results in a value between 0 and 1, where the maximum value of 1 indicates perfect circularity. The fibre cross sections were more circular and thus possessed a ratio close to unity, while other non-circular shapes in the binary image had a lower value. The circularity of each individual object in Figure 2-3 (top) was calculated and the objects with circularity below 2 percentiles of all objects were removed. This approach removed almost all of the non-circular shapes, however some of the approximately circular shapes that were not related to fibre cross sections still remained in the binary image. To eliminate these objects, the orientation of each individual object was calculated. Orientation is defined as the angle between the major axis of the object and x-direction in the image (horizontal direction in the binary image). Since the fibres in the composite were oriented in nominal directions of 45° and -45° with respect to the Y-Z plane (normal plane to microscope images), the shape of their cross section was semi-elliptical. The direction of the major axes of these semi-elliptical shapes (on the X-Y plane) is close to X-axis of the image, which means their orientation angle was close to zero. Obtaining the orientation angle for all objects in the binary image revealed that objects not related to fibre cross sections had larger orientation angles, and there were less of these than objects related to fibre cross sections. These few objects were easily filtered out by

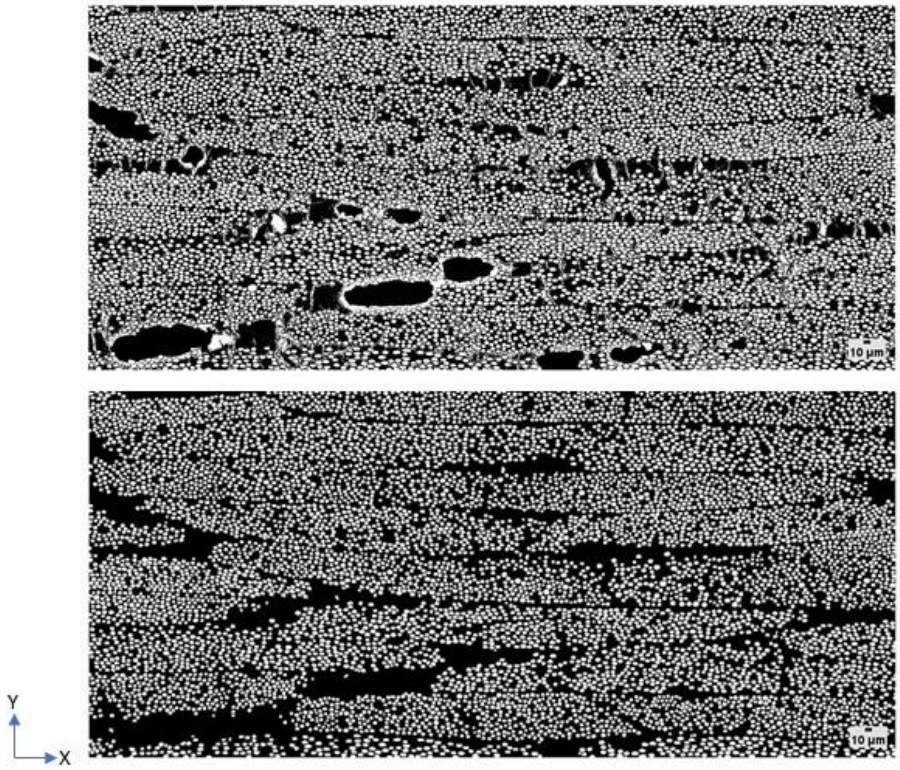

Figure 2-3 Binarized image to separate high intensity regions (notice the noncircular regions surrounding voids and shrinkage cracks distinguishable from circular fibre cross sections) (top), and binarized image with separated high intensity fibre cross sections (bottom).

removing the objects within the top 5 percentiles of orientation values in the binary image. This yielded a new binary image which was again processed using morphological opening to remove the remaining noise, and a typical final outcome is presented in Figure 2-3 (bottom), wherein fibre cross sections have been separated from the matrix and void phases.

2.4 Segmentation of the matrix rich zone

The fibres and voids had already been identified in separate binary images wherein fibre cross sections and voids had the value of 1, respectively. These binary images were summed to get an image wherein both fibres and voids had the value of 1 and the pixels related to matrix had a value of 0. By using an inverse mask, the matrix region became 1 while the pixels of fibres and voids became 0. Although the matrix material was separated, another image processing technique was performed on the binary images to extract matrix rich zones in the structure.

It can be assumed that each fibre in the composite structure reinforces its surrounding matrix, therefore an image processing method must be used to identify the reinforced matrix phase in between adjacent fibres and to assign a portion of it to each individual fibre. These portions of matrix will be called matrix segments. To extract these matrix segments, the binary image in Figure 2-3 (bottom) was inverted to assign zero values to the fibre cross sections. Then the foreground region (matrix and void phases) was eroded successively using the skeletonization method which helped to get a thin skeletonized image. An inverse mask was applied to this skeletonized image and it was summed with the inverse of the binary image in Figure 2-3 (bottom). The result is shown in Figure 2-4 (top) wherein each individual fibre is surrounded by a matrix segment. At this stage, void regions were also added to Figure 2-4 (top), and a convex hull was defined for each individual matrix segment. Since each matrix segment surrounds a zero-intensity fibre cross section, its actual area will be less than the area of its enclosing convex hull. Ideally for each separate segment shown in Figure 2-4 (top) the ratio of these two areas will be close to the volume fraction of matrix in the composite (about 40% in this study). Hence, if the calculated ratio of the areas was less than 40%, then that segment of matrix was identified as being a matrix rich zone as shown in Figure 2-4 (bottom).

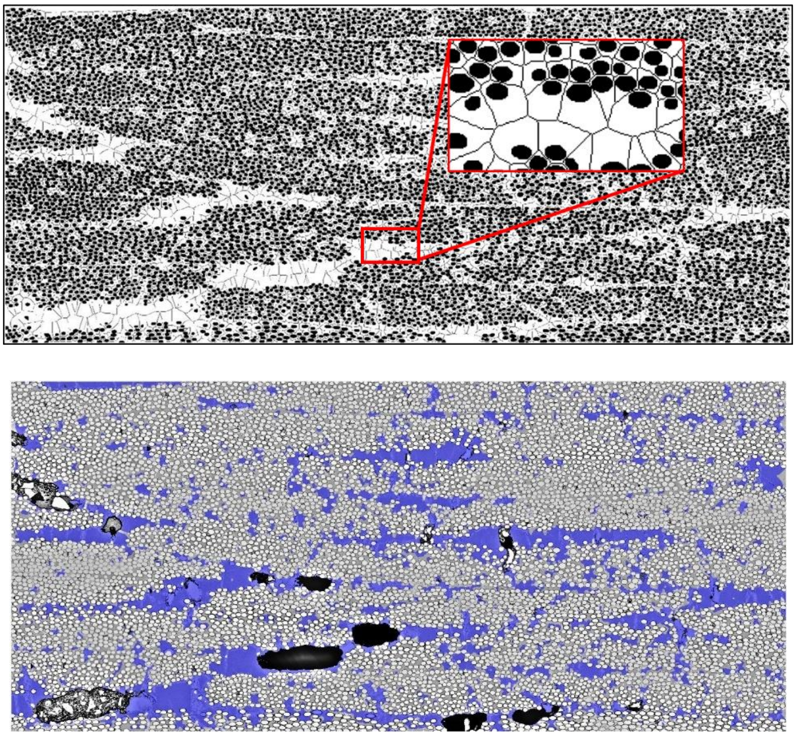

Figure 2-4 Skeletonized binary image with individual matrix segments shown in the inset (top), overlaid image of matrix rich zones on the micrograph (bottom). Image scale as shown in Figure 2-3.

2.5 Extraction of fibre orientation data using digital image correlation

The micrographs of the CMC sample had a similar texture to the speckle patterns used in digital image correlation (DIC) for full-field measurement of displacements. Therefore, the series of micrographs were imported into a commercially-available DIC package (Istra 4D, Dantec Dynamics, Germany), and then each mosaic in the z-direction was processed using the commercial DIC package [12]. The appropriate size of subset for efficient correlation was explored and the results shown in Figure 2-5. It can be seen that small subset sizes significantly reduce the correlation success rate, whereas large subset sizes reduce the resolution of the data. Therefore, image correlation was performed using a subset size of 39×39 pixels to ensure a correlation success rate above 90%. This resulted in a set of 99 displacement fields describing how the fibre locations changed between each mosaic image. The orientation of each layer in the composite was obtained by calculating the inverse tangent of the ratio of the depth difference between consecutive images to the displacement of the fibres in the x-direction. To ensure that localized fibre misalignments did not affect the orientation data, the inverse tangent was calculated between every fifth image. The total displacement in the x-direction was calculated by subtracting the x-displacements of the n^{th} and $(n+5)^{th}$ images. Since the through the thickness distance between consecutive pairs of micrographs was equal to 1 µm, the distance between the 1st and the 5th images based on the window size was set to 4 µm. A typical final result of an orientation calculation can be seen in Figure 2-6, where distinct composite plies have been separated with high resolution. The small abnormalities in the orientation map correspond to the location of voids in the structure.

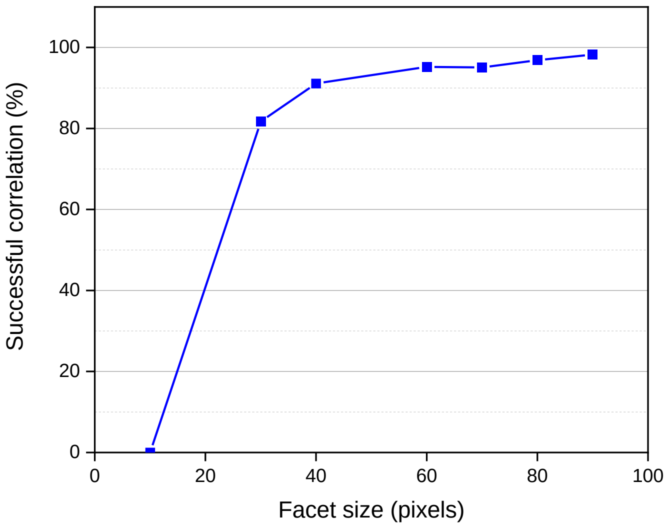

Figure 2-5 Plot showing the decrease in successful correlations as subset size is reduced.

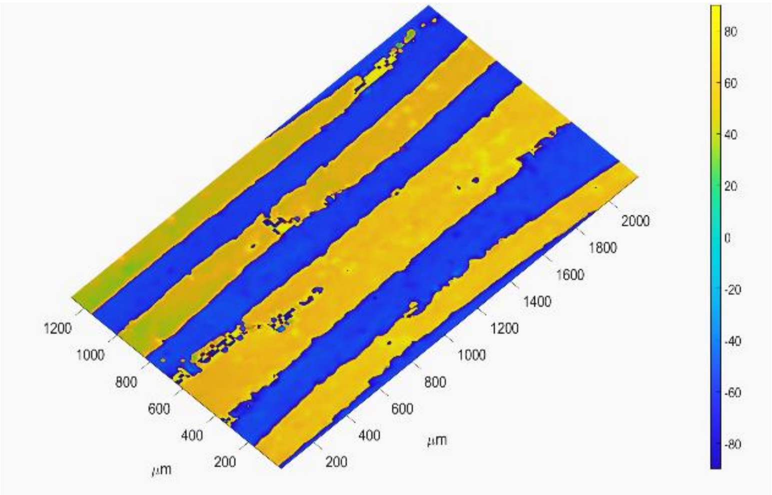

Figure 2-6 The resultant fibre-orientation field after processing (colour bar values show fibre orientation in °)

2.6 Merging of microstructural features

The voids and matrix rich zones (MRZs) were reconstructed straightforwardly in three dimensions by using the outputs of the image processing operations described in sections 2.3 and 2.4. Each individual void and MRZ was labelled and its volume was calculated in terms of the number of voxels used to describe it. Table 2-1 shows the five largest MRZs and voids in the dataset. These accounted for more than 50% of the cumulative volume of all voids and MRZs respectively. The MRZs have complex shapes consisting of columnar substructures attached to chunks of matrix at random locations. A comparison of MRZs amongst themselves revealed that MRZ 1, 2 and 5 are predominantly elongated in one direction and are likely related to matrix accumulations between adjacent plies of the composite, representing an interlaminar matrix. On the other hand, MRZ 3 and 4 do not possess an elongated structure and instead consist of a large chunk of matrix with few substructures attached to them. This type of MRZ appears to be related to cross-over regions between the tows of the composite material, and they are usually adjacent to void defects in the same region [17]. The structure of voids is generally simpler than for MRZs with solid shapes. Their sphericity and orientation within the materials have been discussed thoroughly in a previous study of the same data by Christian et al. [15].

Figure 2-7 depicts the location of the five largest MRZs and nine largest voids superimposed on the fibre orientation map. Nine voids are presented in the figure to show the spatial distribution of more than 99% of the volume of voids in the vicinity of the five largest MRZs. Each microstructural object is labelled with a number which shows its size rank in its category. It can be seen that six of the largest voids are located adjacent to MRZs, which suggests a close relationship between large MRZs and voids in this type of CMC material. Due to the capillary effect during polymer infiltration and pyrolysis, voids tend to form at regions where the fibres are more loosely packed [18]. These loosely packed regions such as tow cross over locations in the CMC microstructure are partially filled by matrix material during the infiltration and create matrix rich zones. Therefore, the presence of large voids in the vicinity of MRZs can be related to manufacturing process parameters which might cause simultaneous creation of voids and MRZs in the microstructure.

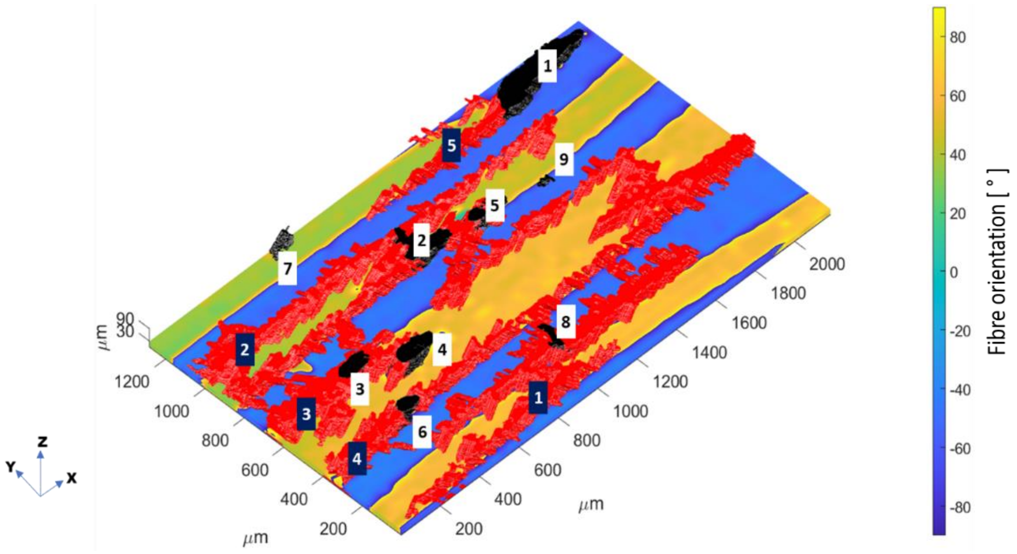

Figure 2-7 Merged presentation of the largest voids (black features) and MRZs (red features) with the numbers indicating the rank of the object in terms of its size. The features are superimposed on the fibre orientation map for the sample.

Table 2-1 The volumetric representation of the five largest MRZs (middle column) and five largest voids (right column) in the sample. Notice the interlaminar columnar morphology of the 1st, 2nd and 5th MRZs as compared to the less complex structure of the 3rd and 4th MRZs. All voids are smaller in size and have simpler morphologies than the MRZs.

Size Rank	MRZ	Void
1	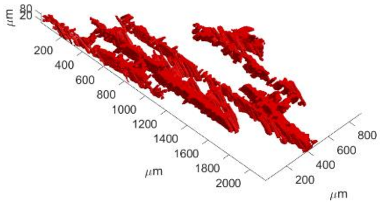	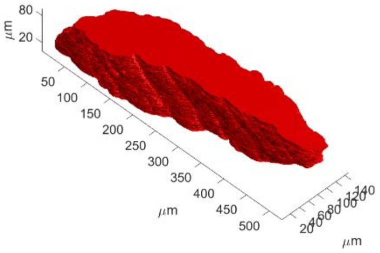
2	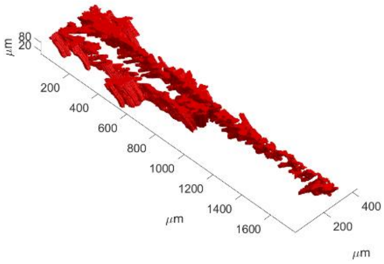	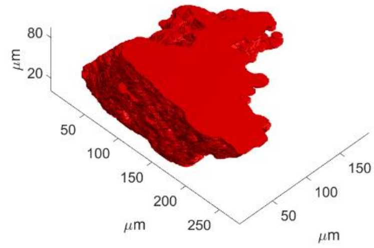
3	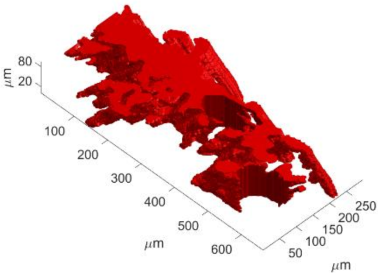	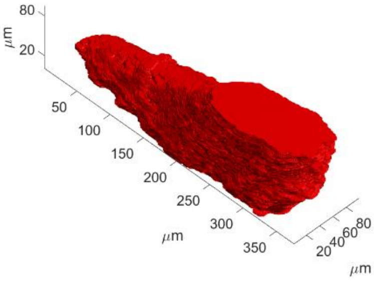
4	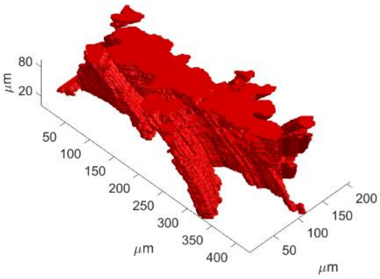	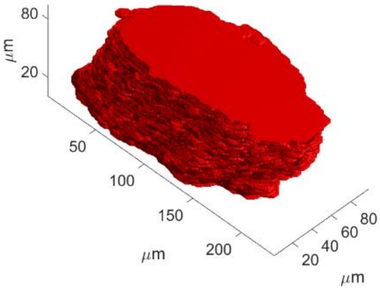
5	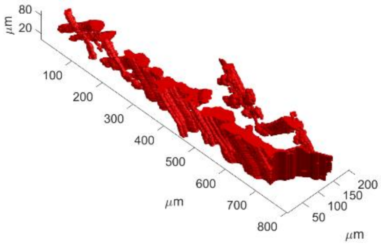	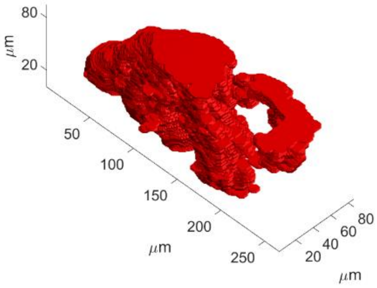

2.7 Volume decomposition of microscopic features and their reconstruction

Characterizing the volumetric data of the microstructural features was performed using the volume decomposition technique developed at the University of Liverpool [14]. In this method, three-dimensional kernels of the Chebyshev polynomials are used to decompose volumetric data arrays. The volume decomposition procedure results in a feature vector f, that contains the coefficients of the Chebyshev polynomials used to approximate the spatial data of the volume. Since the dimensionality of the volumetric data array is reduced to a vector, comparison of any two volumetric arrays can be accomplished simply through evaluation of their feature vectors. Moreover, the decomposed volumes can be reconstructed using its feature vector to ensure that it is an appropriate representation of the original data which can be evaluated using the root mean square error.

Each individual object in the 3D microstructure can be decomposed using volume decomposition, but keeping all of the coefficients in the feature vector can still mean that the level of data dimensionality is high. This is because not all coefficients have a high enough magnitude to significantly affect the reconstruction of the object. These insignificant coefficients can be filtered out by retaining only the largest coefficients. To find the minimum number of significant coefficients, the root mean square error of the object's reconstruction can be plotted against the number of significant coefficients. The minimum required number of coefficients can be set as the point at which there is a rapid increase in the slope of the root mean square error (RMSE) as the number of significant coefficients is decreased. For example, the appropriate number of significant coefficients for the 4th biggest MRZ, consisting of more than 2.2×10^6 voxels, was 300, as shown in Figure 2-8 (top). The plot of the root mean square error shows that the steep gradient gradually becomes shallower as the number of retained coefficients goes over 300. The reconstructed volume of the same MRZ is depicted in Figure 2-8 (bottom). The main shape features of the MRZ were found to be well reconstructed using a feature vector containing just 300 non-zero coefficients, resulting in a RMSE reconstruction error of about 0.25 voxels.

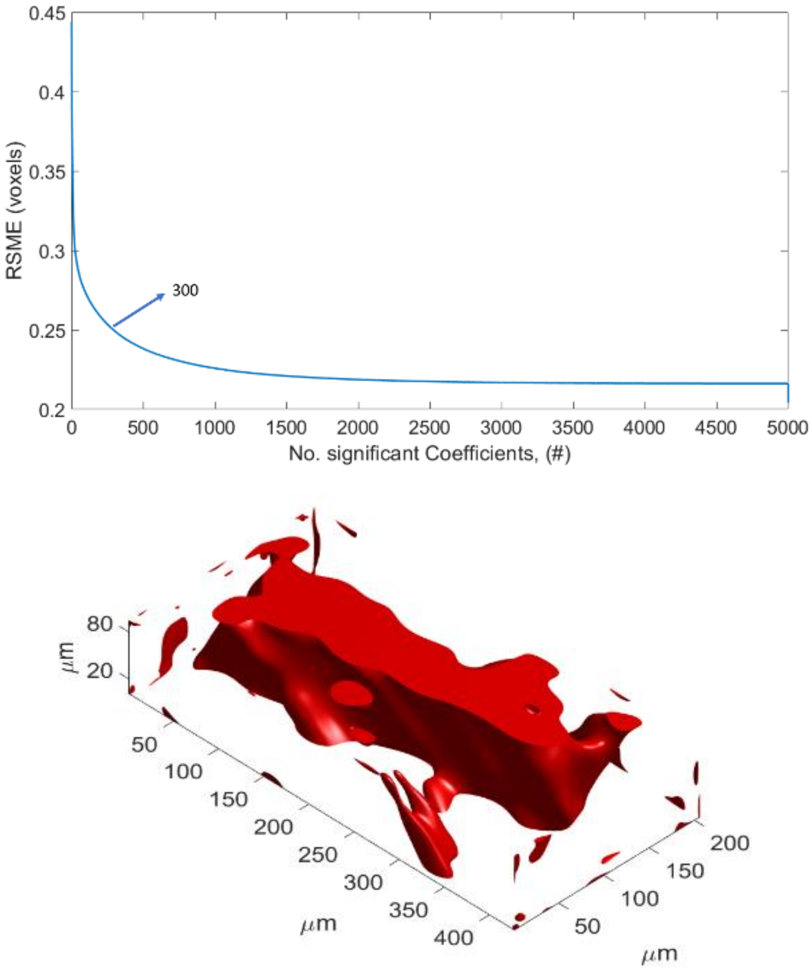

Figure 2-8 Decrease in root mean square error of reconstructing the volume data with the increase in number of significant coefficients (top), the reconstructed volume of the 4th MRZ using 300 significant coefficients based on observations of the above plot.

2.8 Significant coefficients projecting the main geometric features of microstructural objects

Since three-dimensional kernels are used to decompose volumetric data arrays, the kernels corresponding to significant coefficients obtained from volume decomposition exemplify the characteristics of the 3D object. Figures 2-9 (top left) and 2-8 (top right) represent the 123rd largest MRZ in the composite material and its reconstructed volume, respectively. The actual microstructural object consists of two columnar overlapping substructures with different orientations which creates a cross shaped object. The volume decomposition of the object reveals that the three largest absolute value coefficients in feature vector correspond to kernels 1, 5 and 74. Among these three coefficients, the 1st coefficient can be ignored when considering shape as it represents volume of the object. The 5th and 74th kernels, which indicate shape characteristics of the MRZ, are shown in Figure 2-9 (bottom). The 5th kernel indicates the MRZ is orientated on the Y-Z plane and the 74th kernel contains the cross pattern visible on the same plane. By performing this analysis on other MRZs it is possible to identify the significant coefficients that indicate the major shape characteristics of the spatial data, and a comparison of the resultant feature vectors allows the relationship between two objects to be quantified.

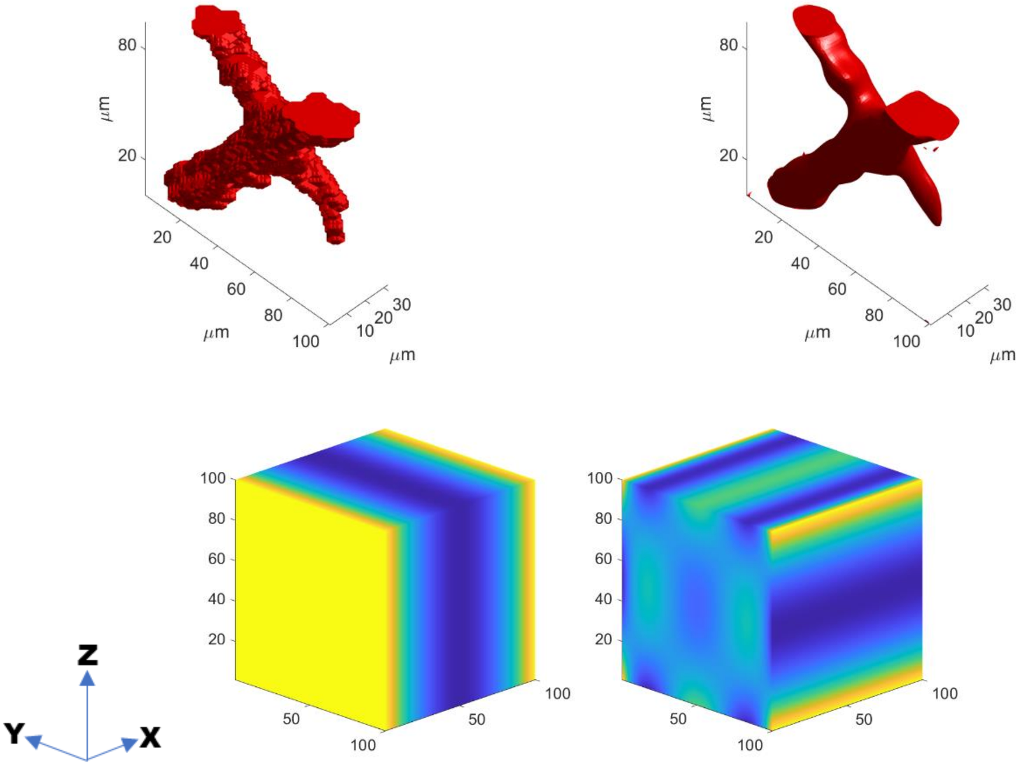

Kernel 5 (left) and Kernel 74 (right)

Figure 2-9 Presentation of the 123rd MRZ (top left), reconstructed MRZ with significant coefficients (top right), kernels related to second (bottom left) and third (bottom right) most significant coefficients of the feature vector used to reconstruct the MRZ

2.9 Shape comparison through hierarchical clustering

The similarity of two MRZs can be determined by calculating the Euclidean distance between the feature vectors describing those MRZs. Figure 2-10 shows a heat map representing the similarity of each MRZ to all other MRZs (for the 200 largest MRZs, arranged in descending volume).

The MRZs have been clustered using non-global bottom to top agglomerative hierarchical clustering, where each MRZ is initially treated as a single cluster. The two closest clusters, as defined by the Euclidean distance between their describing feature vectors, are then merged. This process was repeated until all MRZs were clustered. Three major clusters were identified, corresponding to interlaminar, intralaminar and tow cross MRZs respectively. The heat map of Figure 2-10 has been rearranged to group similar MRZs in Figure 2-11, where these three clusters are identified with a dendrogram plot. By automating the classification of MRZs into morphological categories, the workload required for engineers to process and interpret large volumetric datasets can potentially be reduced. This could make it easier for specific microstructural features that are known to affect the performance of a composite to be quickly found and studied.

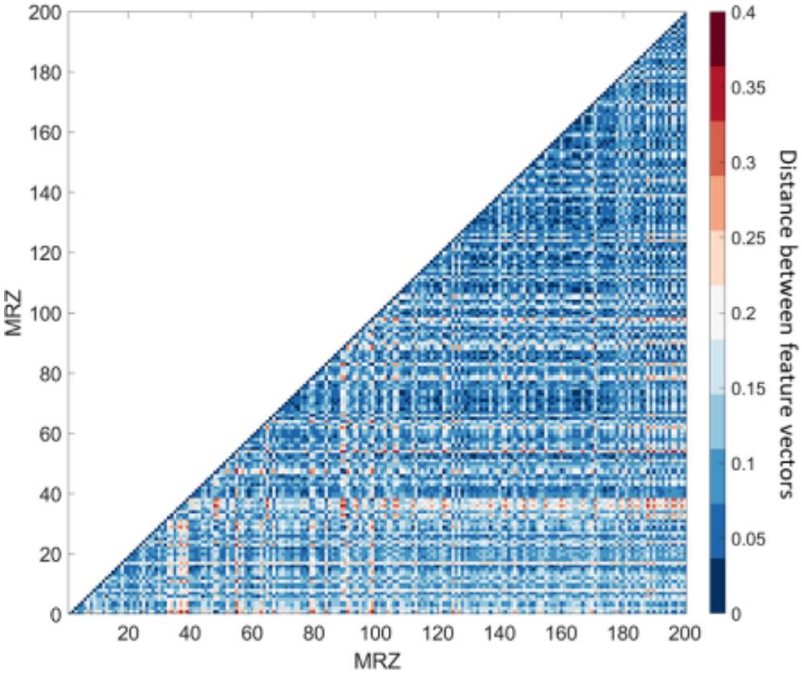

Figure 2-10 Heat map indicating the similarity of each MRZ to every other MRZ for the 200 largest MRZs. MRZs arranged from largest to smallest, MRZ 1 is the largest identified. Blue indicates high similarity, red indicates low similarity.

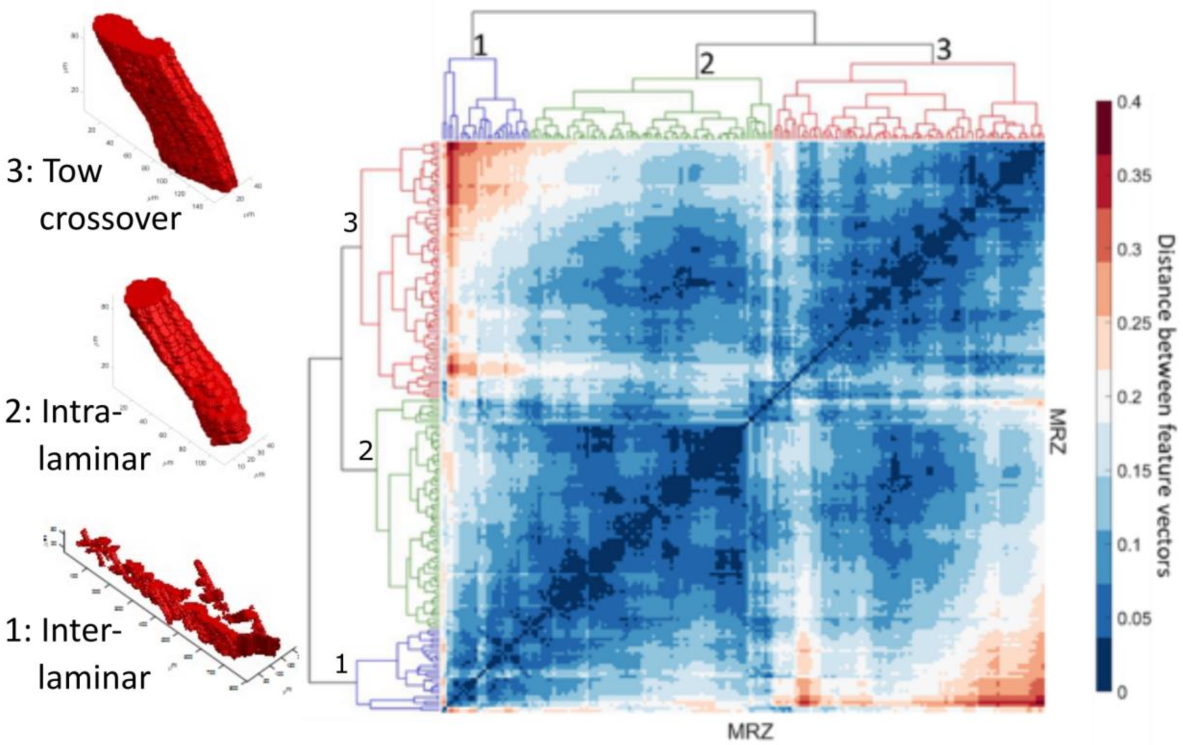

Figure 2-11 Heat map of Figure 2-9 rearranged to indicate the three clusters of MRZ similarlty, with the blue dendrogram identifying interlaminar MRZs (1), the green intralaminar MRZs (2) and the red tow crossover (3) MRZs. Exemplars of the three identified categories are shown inset left.

3. Application of orthogonal decomposition to volumes of measurements to characterise three-dimensional microstructures based on computed tomography data

The section describes the research performed in pursuit of objective (b) To apply orthogonal decomposition to volumes (tensors) of measurements to characterise three-dimensional microstructures based on computed tomography data.

3.1 Datasets

Tomography data of minicomposite specimens at four different tensile loads (40, 80, 120 and 160 N) were provided by AFRL as sets of .tiff files. The minicomposites contain SiC fibres coated with boron nitride, with an overlayer of SiC matrix. The images can be stacked to represent the full three-dimensional volumes, and damage can be visually identified in these images (Figure 3-1).

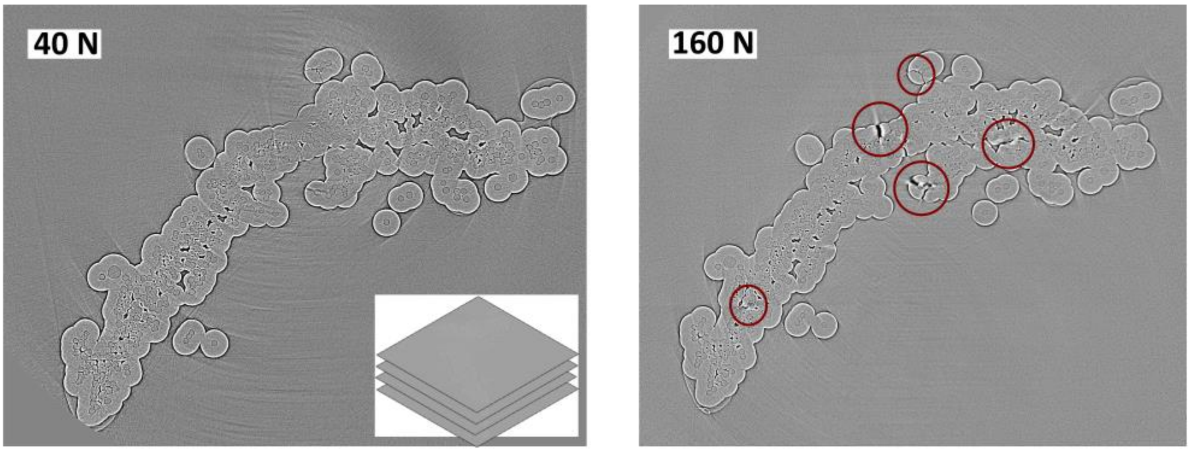

Figure 3-1 First tomography slice from datasets at 40 and 160 N, inset indicates stacking of slices to reconstruct the three-dimensional dataset. Red ovals indicate damage visible at 160 N, which has either appeared or extended with respect to the image at 40 N.

Previously, location and tracking of damage using orthogonal decomposition of two-dimensional datasets (images) has been carried out [13, 15], here this approach is extended to three-dimensional datasets. Two approaches to processing these datasets using volume decomposition have been investigated: (1) identifying individual fibres and locating damage along their length; (2) a coarser bulk approach, which identifies differences due to damage in three-dimensional space.

3.2 Processing of individual fibres

An algorithm has been developed to detect fibres within an image using an orthogonal decomposition approach. This requires initial input of a number of manually identified fibres, which are then decomposed to determine a “median” fibre. The algorithm then locates similar regions in the images, and identifies them as fibres. The details of this process are shown in Figure 3-2. This algorithm identified 83% of the 114 fibres present (i.e., 19 false negatives), and generated 13 false positives in a selected region in the first image of the 40 N dataset.

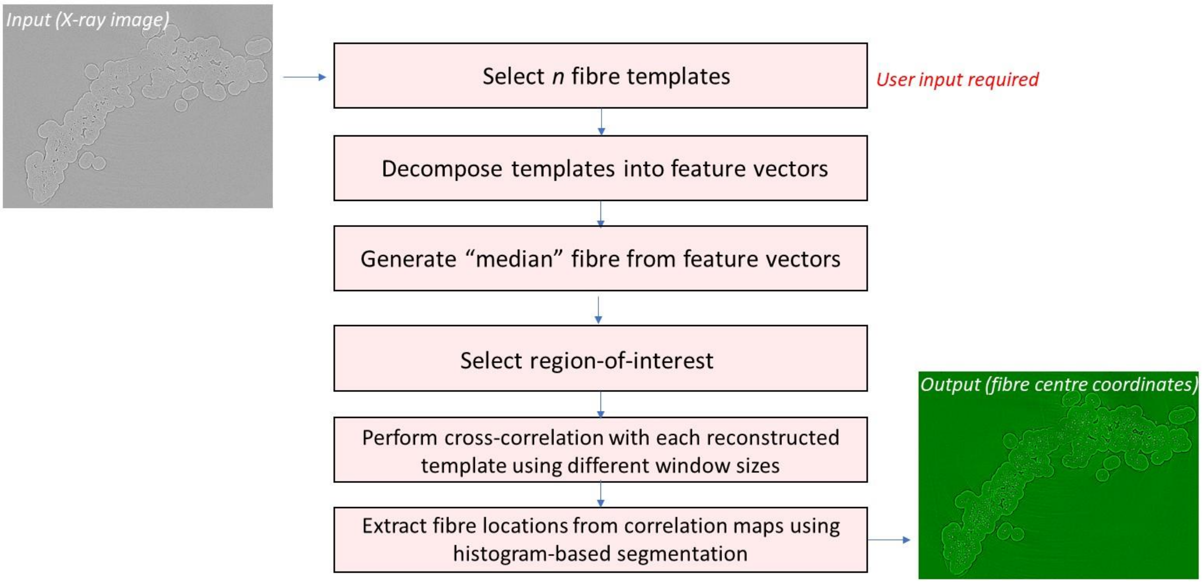

Figure 3-2 Flowchart describing the fibre detection algorithm.

Once a fibre has been identified in the first image of one of the datasets, either using an automated approach or manually, a separate algorithm has been developed, which automatically locates that fibre in both datasets. In this way, fibres and their immediate surroundings were extracted from both datasets as volumes which were then compared using decomposition (Figure 3-3).

These datasets were segmented into sub-volumes, which were decomposed to generate feature vectors for a given height in the tomography data. Using a rolling calculation, where the (n+1)th sub-volume was offset from the nth sub-volume by one pixel in the z-direction, the difference between the feature vectors was calculated, and can be seen in Figure 3-3. Increases in the vector difference at given depths in the dataset can be linked to visually observed damage in the higher load dataset.

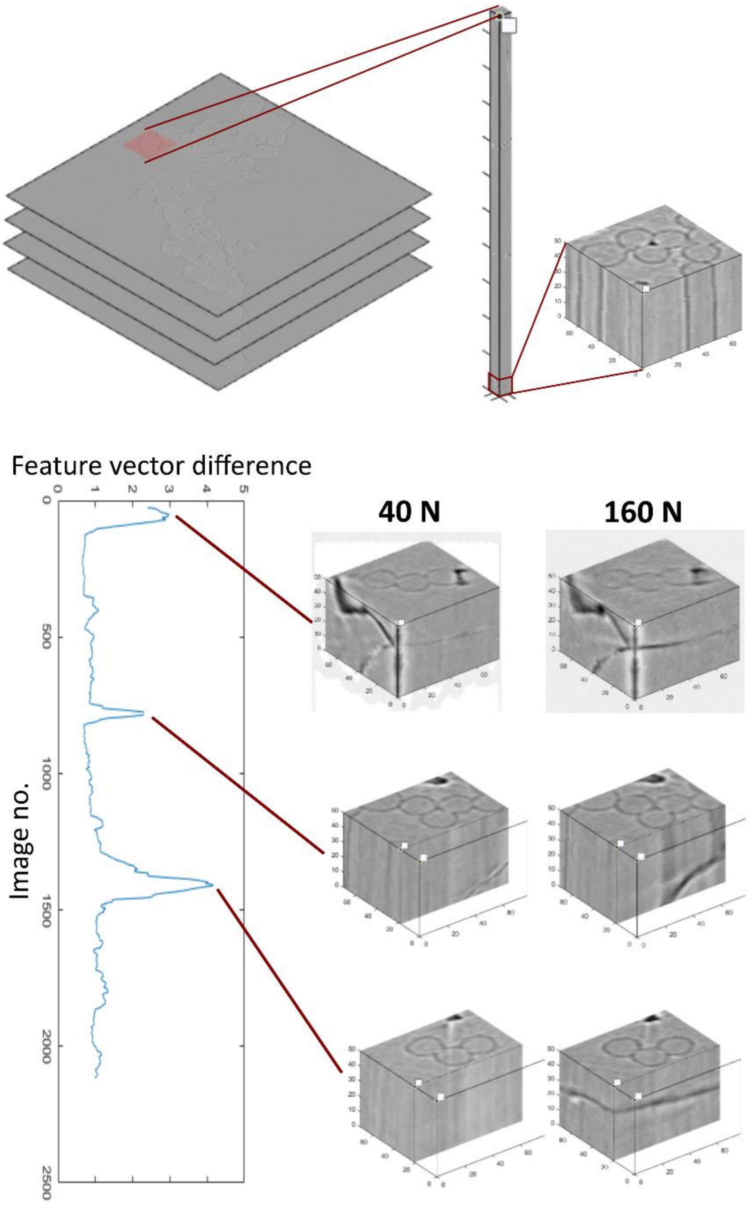

Figure 3-3 Data processing and feature vector results for one individual fibre. Extracted sub-volumes measure 50 pixels in height.

3.3 Processing of larger volumes

A similar volume decomposition approach has been carried out on a larger subset of the tomography data, providing location information for damage in all components of the specimen, at larger length-scales than seen in the individual fibres.

In order to carry out a comparison between the datasets, datasets were aligned in three-dimensional space, so that equivalent x-y-z positions were interrogated. Here, the initial alignment and data cropping was carried out manually. A 500 x 500 px square region was identified for use as a proof-of-concept region of interest from the lowest and highest load datasets. This region of interest contained a large number of fibres, very little air, and damage that could be visually observed in the 160 N dataset (Figure 3-4).

This region of interest was extracted from the individual .tiff files to generate two stacks, from 40 and 160 N respectively (Figure 3-4). Differences between the two datasets can be visually observed, where cracks have developed or extended at the higher load.

Figure 3-4 also details the process of comparing these datasets using volume decomposition:

1. Stacks are divided using a 3D grid, to generate sub-volumes of the same dimensions (100 x 100 x 100 px).
2. Each sub-volume is independently decomposed to generate a feature vector.
3. Feature vectors at equivalent x-y-z position are compared to quantify the differences.

By overlapping the sub-volumes in the x, y and/or z direction, it is possible to generate a higher resolution picture of the differences.

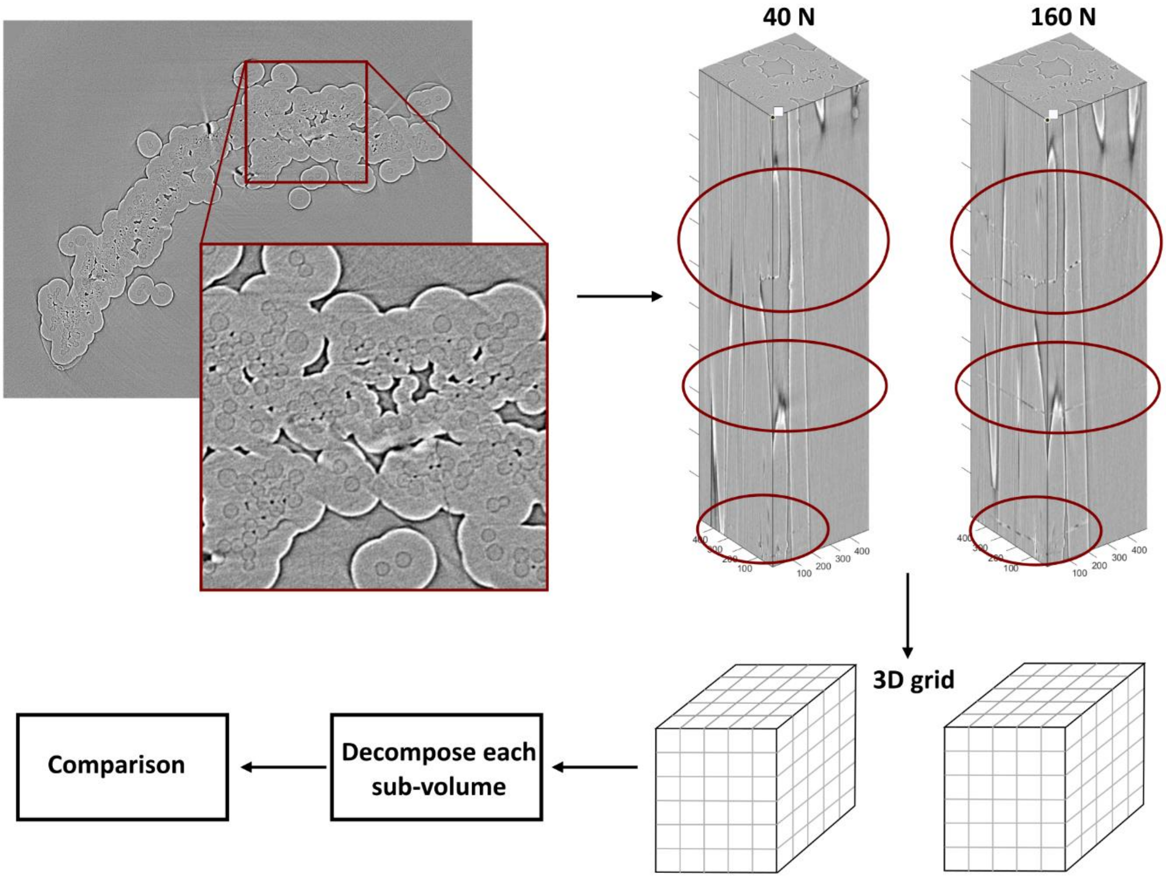

Figure 3-4 Steps used in volume decomposition of bulk specimen. Region of interest measures 500 x 500 pixels.

3.4 Filtering of feature vectors

When carrying out a comparison between the feature vectors, filtering of the coefficients is sometimes carried out, either because they are very small and therefore are below a significance threshold [19, 20], or because the shape they represent is not of interest during the comparison [13]. Here, the shape represented by coefficients was considered, and feature vectors were filtered to remove coefficients which correspond to kernels containing the zeroth or first order polynomials. This filtering removed effects due to the magnitude of the original datasets and unidirectional gradients in the data respectively.

Difference maps calculated from feature vectors with no filter, and three filter options are shown in Figure 3-5. It can be seen that features in the difference maps become more apparent when the filtering has been applied.

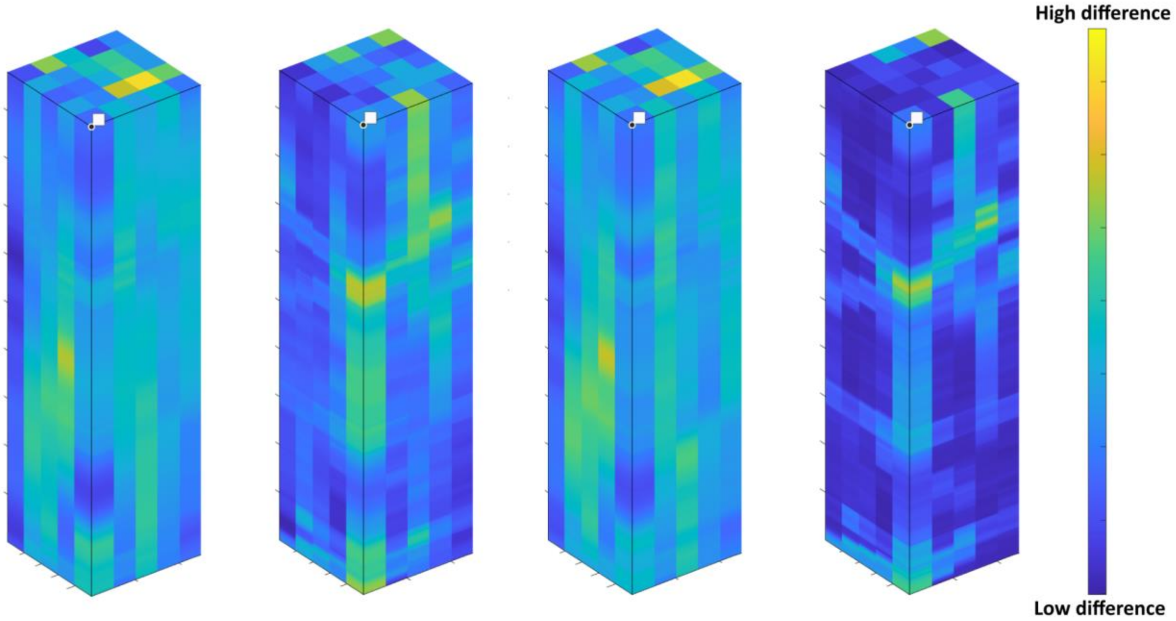

Figure 3-5 Comparison between the feature vector difference maps when calculated with (left to right) unfiltered feature vectors; feature vectors with the zeroth order polynomials removed; feature vectors with the first order polynomials removed; and feature vectors with both the zeroth and first order polynomials removed.

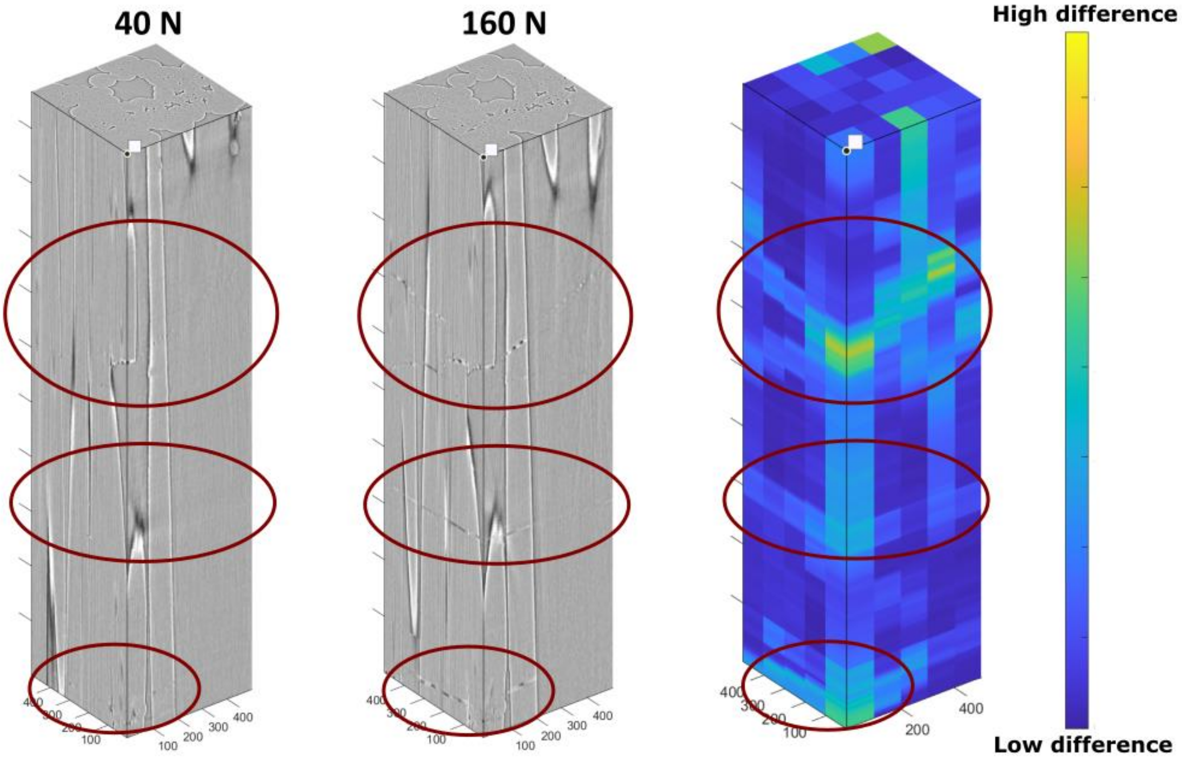

Figure 3-6 Stacked tomography data at 40 N and 160 N and feature vector difference map between the two loads. Red ovals indicate substantial extension of damage visible in the higher load dataset, which can also be seen in the feature vector difference map.

3.5 Feature vector difference results

Figures 3-6 and 3-7 show the results of comparison between the two datasets using the volume decomposition approach. The sub-volumes used to generate the feature vectors were overlapped in the z-direction (height), but not in the x and y direction i.e., a coarse resolution in the x and y direction, and a fine resolution in the z direction. A fine resolution in z was chosen as this was parallel to the loading direction and was consistent with the approach used for individual fibres in Section 3.2. The vector difference showed regions of higher difference, the locations of which correlate qualitatively with positions where cracks can be visually observed in the tomography data.

This comparison is extended in Figure 3-7 with slices through these datasets, where cracks in the 160 N dataset are indicated by areas of higher magnitude in the vector difference maps.

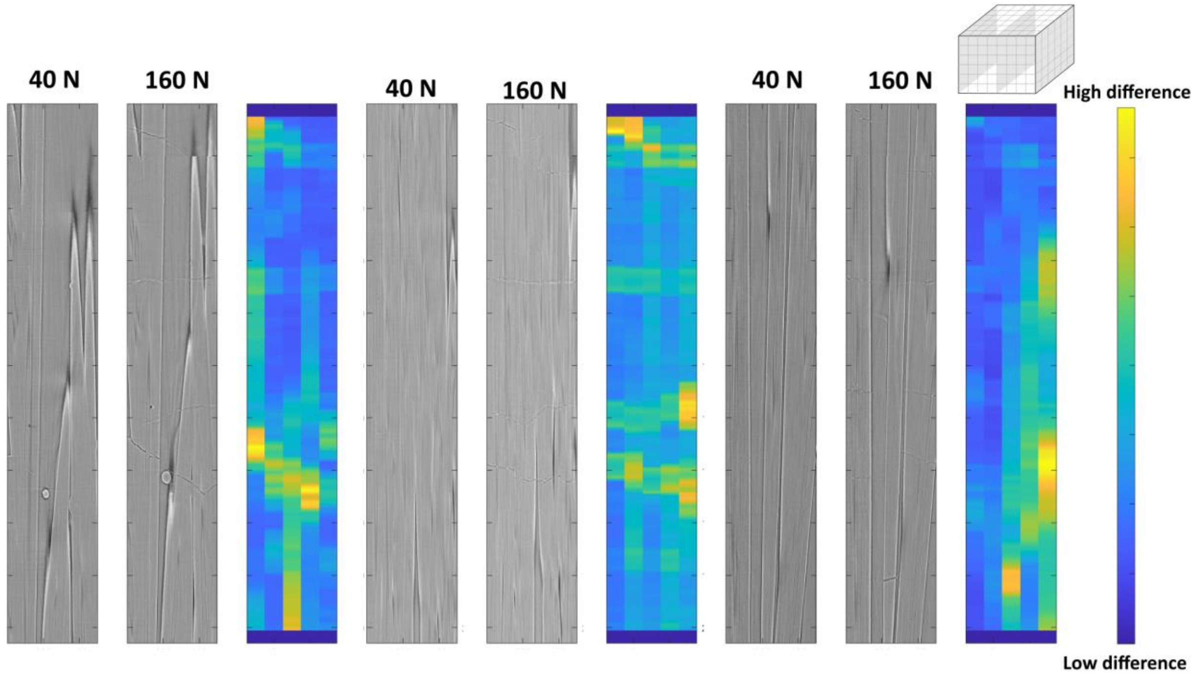

Figure 3-7 Slices through the volumetric data shown in Figure 3-6.

3.6 Grid resolution

As seen in Figures 3-6 and 3-7, higher resolution difference data can be achieved by overlapping sub-volumes used in the feature vector calculations. However, if applied in all directions to a large volume, this “rolling” approach becomes computationally expensive as large numbers of sub-volumes must be processed and the resultant feature vectors saved. This approach therefore removes one of the major advantages of orthogonal decomposition of images or volumes, which is the ability to represent large amounts of data using feature vectors which are orders of magnitude smaller than the original data.

It is possible to compare overlaps of different offsets, to determine a compromise between the required resolution and the processing time. Table 3-1 shows the relative computer processing time for a range of resolution options. The vector difference results are shown in Figure 3-8, showing that even at the coarsest resolution, some indicators of damage are present. These indicators become more evident, and damage location information more apparent, at higher resolutions.

Table 3-1 Relative computational time required for a range of grid resolutions.

	X overlap	Y overlap	Z overlap	Number of coefficients (unfiltered)	Computation time (approx.)
1	0	0	0	10 000	20 seconds
2	0	0	99	10 000	45 minutes
3	50	50	50	10 000	3 minutes
4	75	75	75	10 000	23 minutes
5	90	90	90	10 000	> 4 hours

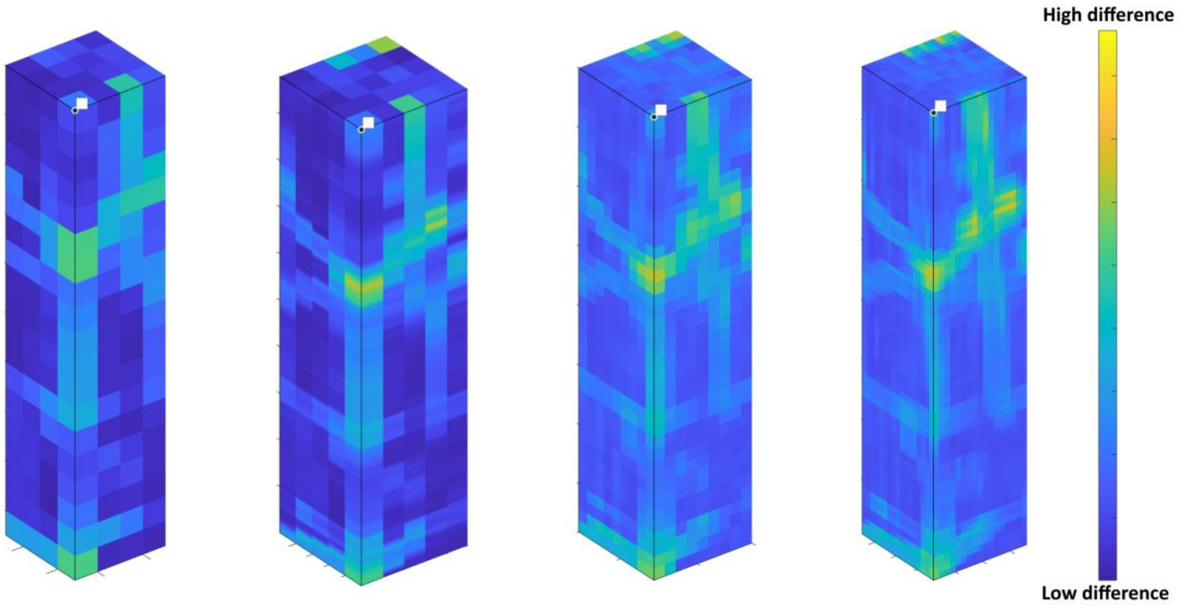

Figure 3-8 Vector difference maps for four of the grid resolutions in Table 3-1. (Left to right; 1, 2, 3, 4).

3.7 Intermediate loads

The progression of damage with increasing load can be seen when analysing the intermediate datasets in the same way that comparisons between the 40 and 160 N datasets were made. For this comparison, a smaller subsection of the volume described in Section 3.3 above was used, to minimise the presence of air in the datasets, and limit artefacts due to edge-effects found when fibre edges were unconstrained (Region of Interest (RoI) 1 in Figure 3-9).

This sub-volume was manually identified in the four tomography datasets, and the feature vector difference calculated between the 40 N dataset and all subsequent loads, using the bulk volume approach described in section 3.3. Figure 3-10 shows the extracted tomography stacks for each load, and the results of the feature vector difference calculations. It can be seen that increased damage is visible in higher load tomography datasets.

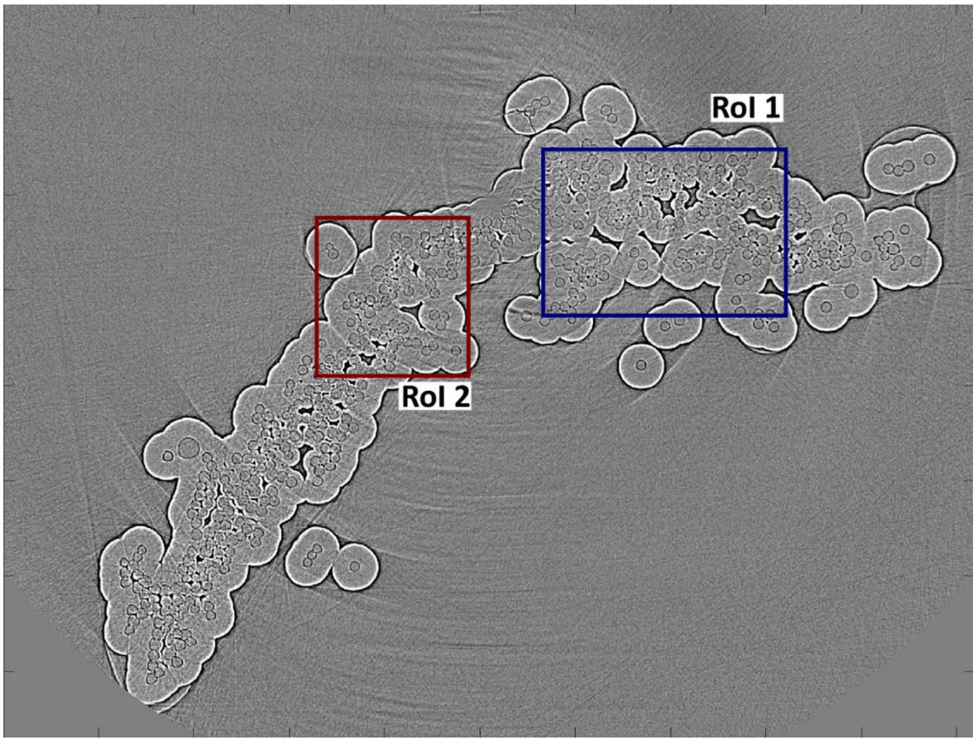

Figure 3-9 First tomography slice of 40 N dataset. Blue and red rectangles indicate the two regions of interest (RoI) extracted from all slices for bulk volume decomposition, RoI 1: 300 x 475 pixels, RoI 2: 335 x 280 pixels.

Regions of high feature vector difference align with the damage visible in the tomography datasets, and the magnitude and size of these concentrations increase with increasing load, indicating the increase in damage. An alternative visualisation of the feature vector difference between the 40 and 160 N datasets is also shown in Figure 3-10, where three-dimensional contours link positions of the same feature vector difference. These contours enclose areas of higher feature vector difference, therefore indicating the shape of high difference concentrations or damage.

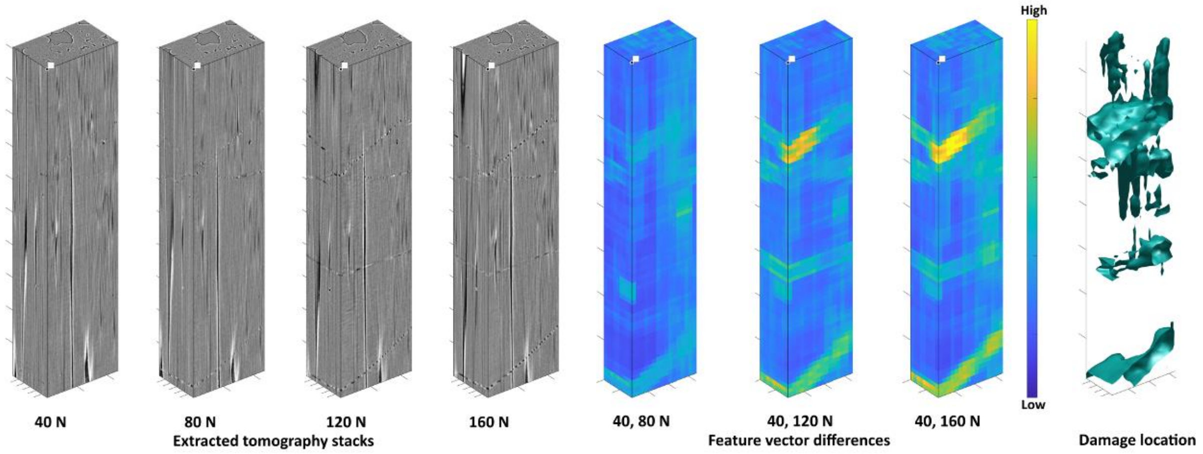

Figure 3-10 Extracted tomography stacks for RoI 1 at the four load cases (left); feature vector differences calculated between the lowest load dataset (40 N) and subsequent datasets (centre); internal morphology map of indicated damage (high difference) from comparison of feature vector difference between 40 and 160 N datasets (right).

A second region of interest was identified, and the same process was carried out to compare the datasets at the four loads (Figure 3-11). As with the first region of interest, the feature vector difference in areas of damage increased with increasing load, and the internal structure of the indicated damage can be mapped. It should be noted that for both of these regions of interest, there are high difference areas which may be artefacts and not related to damage, e.g. the vertical features in RoI 1, and the high difference at the front, top corner of RoI 2. Although these regions of interest were selected to avoid air as far as possible, the shape of the specimen does not allow for air to be eliminated entirely. Therefore, approaches to exclude or account for these artefacts should be considered in future work.

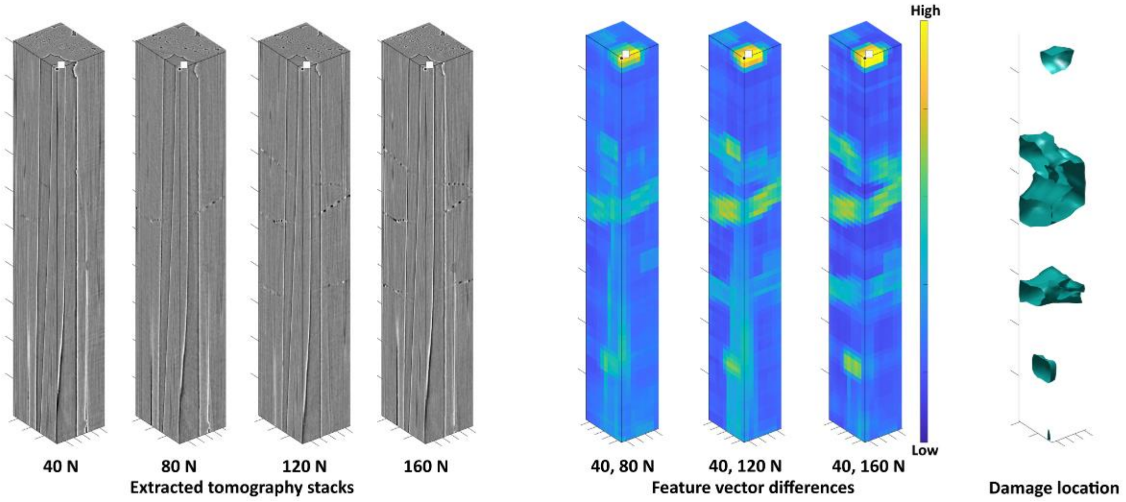

Figure 3-11 Extracted tomography stacks for RoI 2 at the four load cases (left); feature vector differences calculated between the lowest load dataset (40 N) and subsequent datasets (centre); internal morphology map of indicated damage (high difference) from feature vector difference comparison between 40 and 160 N datasets (right).

The morphology of located damage areas within the volume for RoI 1 is also shown in Figure 3-12 with the feature vector differences for individual fibres superimposed on the bulk difference results. It can be seen that high differences calculated by the individual and bulk volume methods coincide, showing that both approaches are indicating damage in the same locations.

The two approaches to using volume decomposition have associated advantages and disadvantages. The higher resolution gained from analysing individual fibres requires higher initial processing power in order to extract those fibres, and information is locally restricted to fibre positions. The bulk approach is quicker and covers a larger volume, but results in a coarser resolution of the damage information. Therefore, when using this volume decomposition technique for damage detection, it is necessary to consider which approach would be appropriate for a given use-case, or if a combined approach may give complementary information.

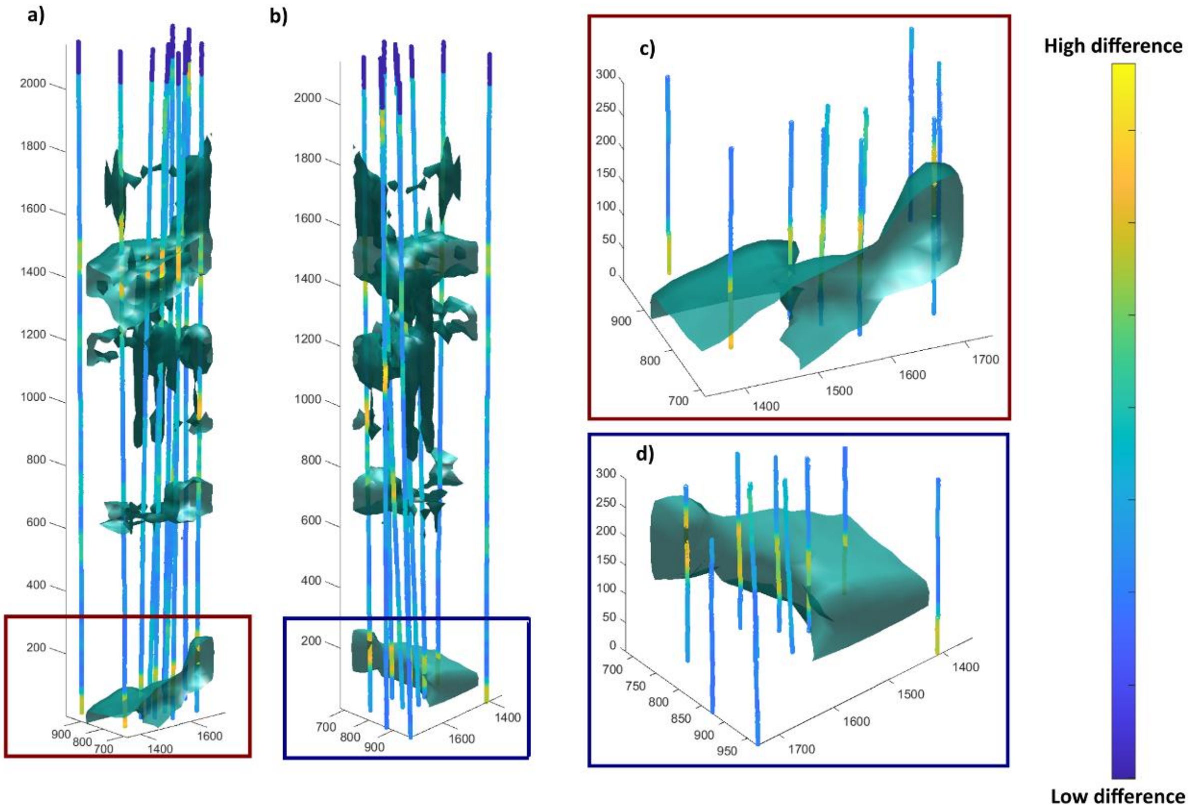

Figure 3-12 Feature vector differences between the 40 and 160 N datasets of region of interest 1 calculated using the bulk and individual fibre approaches. Contours of high feature vector difference from bulk comparisons (green) are overlain by individual fibres, the colour of which indicates the calculated feature vector difference at that position. (a) and (b) show the whole stack from two viewing angles, (c) and (d) show the lower identified damage location from the same viewing angles.

3.8 Fibre interactions and fibre twisting

A further potential use of orthogonal decomposition techniques in tomography datasets is the potential to correlate the microstructure of a specimen with detected damage. This would allow consideration of whether the degree of fibre twisting, and interactions with adjacent fibres impacts the development and quantity of damage. One individual fibre, which shows two areas of significant damage is shown in Figure 3-13. Individual slices from this fibre at 40 N have been decomposed using 2D orthogonal (image) decomposition.

The feature vector difference results from volume decomposition of this fibre are then plotted, along with selected coefficients from 2D orthogonal decomposition in Figure 3-14. Peaks in the feature vector difference are indicative of the damage evident in the tomography datasets shown in Figure 3-13. It can also be seen that the values of individual 2D orthogonal decomposition coefficients change throughout the stack, and it is possible that the behaviour of some of these coefficients is indicative of structural changes such as fibre twist. One of the damage locations indicated by volume decomposition results coincides with locations where the values of coefficients 3 and 6 show significant change (from negative to positive and vice versa, respectively). This correlation is of interest when aiming to analyse the relationship between damage and fibre behaviour or fibre twist.

Linking these changes in shape descriptors to changes in the three-dimensional structure and determining whether there is a relationship to fibre twist is not straightforward. Here, there is damage present at the lowest load, so it would be necessary to differentiate between any effects on the feature vector coefficients from damage and those related to the structure of the specimen, which requires further research. These results show that combining 3D and 2D orthogonal decomposition techniques can provide complementary information on the behaviour of materials. Therefore, the possibility that damage location can be correlated to structural features indicates that the combination of these techniques is an interesting area for further development.

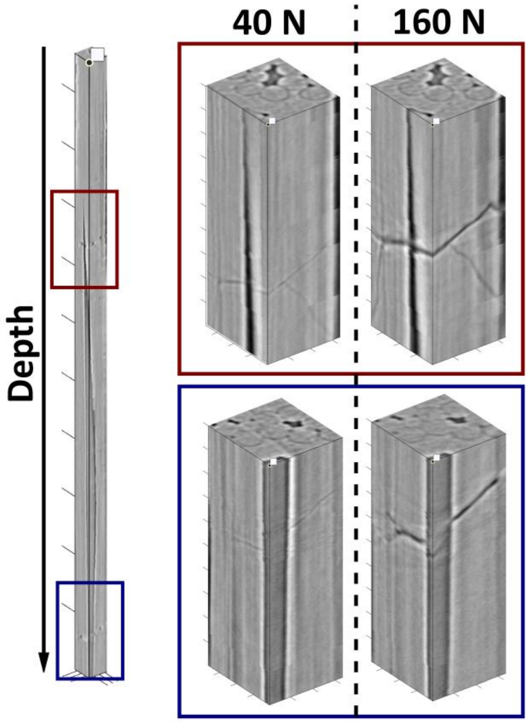

Figure 3-13. One extracted individual fibre tomography dataset. Insets show extracted sub-volumes (200 pixels in height) of the two areas indicated in the full stack where significant damage has occurred between 40 and 160 N.

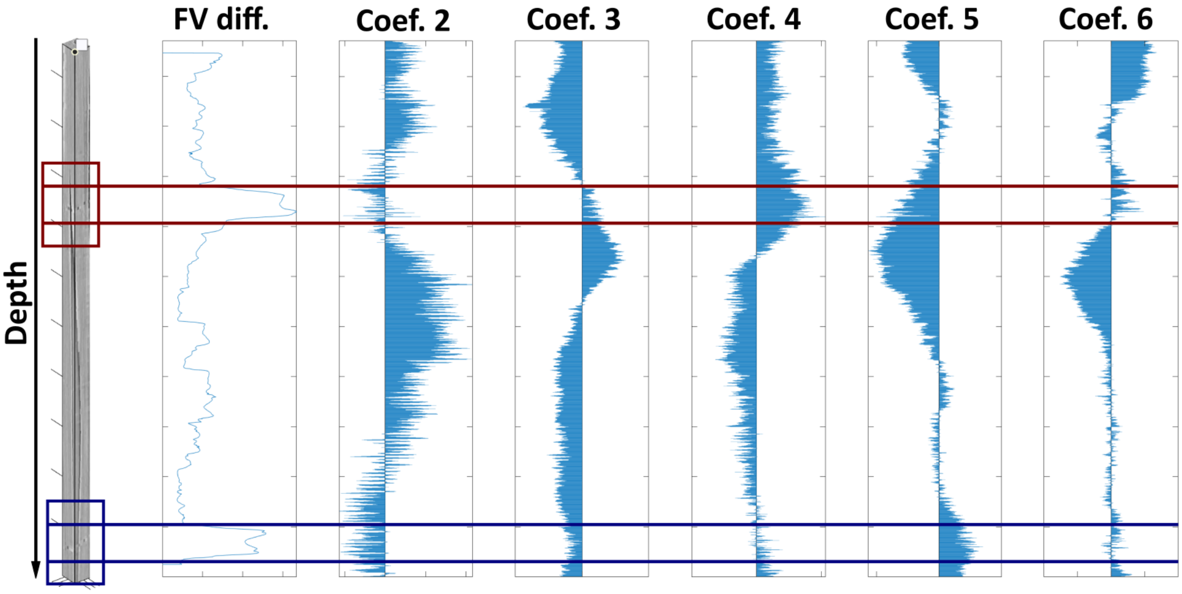

Figure 3-14 3D and 2D orthogonal decomposition results from the extracted fibre shown in Figure 3-13. The increased damage visible in tomography data at the higher load (left), is indicated by peaks in the feature vector difference plot calculated from volume decomposition. Coefficient values have been calculated from two-dimensional decomposition of individual slices in the tomography data at 40 N. Red and blue boxes and horizontal lines indicate the position of significant damage, which can be seen in inset figures in Figure 3-13.

4. Exploration of the effects of loading rate on the development of damage using strain-based measurements described by feature vectors

This section describes the research performed to achieve objective (c) To explore the effects of loading rates on the development of damage using strain-based measurements described by feature vectors.

4.1 Impact tests

Unidirectional carbon fibre prepreg (RP542-4, PRF, UK) composed of T700 12K carbon fibre and epoxy resin was used as the raw material for all specimens. The prepregs were cut into dimensions of 170 mm × 150 mm and a layup configuration of $[0_2/90_2]_{2s}$ was used to create laminates. These laminates were then cured in a hot press (APV-3530, Meyer, Germany) at a temperature of 130°C and pressure of 2.4 bar for 45 minutes. The specimens were naturally cooled down to room temperature with the press closed before demoulding. In total, two CFRP laminates were produced with a nominal thickness of 3.4 mm. These were then cut to the final size of 150 mm × 100 mm using a waterjet cutter. A speckle pattern was sprayed on the surface of the specimens using matte black paint on a white background. The random pattern was applied according to the recommendations for good practice for DIC measurements to ensure the lowest possible noise in the output measurements [21]. The samples were placed on the impact rig as seen in Figure 4-1 where the impact tup would hit the specimen from above.

A mirror was positioned at an angle of 45° beneath the impact rig to enable optical monitoring of the displacements on the bottom surface of the specimens. A stereo digital image correlation (DIC) system (Q-450, Dantec Dynamics, Germany) with high-speed cameras (Photron, Japan) and 100 mm lenses (Carl Zeiss, Germany) was used to measure the displacement fields on the bottom unsupported surface of the specimens during impact tests as shown in Figure 4-1. The cameras were set to a shutter time of 40 μs and frame rate of 10 KHz. The image recording process was triggered using a mounted optical sensor attached to the impact machine that detected the impactor just prior to it making contact with the specimen. Each of the specimens were impacted with an energy of 20 J resulting in a total of 300 pairs of images captured during each test. The full-field deformations were obtained by post-processing the images in Istra 4D (Dantec Dynamics, Germany) using a subset size of 25×25 pixels and subset centre-to-centre distance of 19×19 pixels. During the impacts, force data were also recorded using a load cell integrated into the tup of the impact machine. The strain and displacement fields obtained using DIC were then associated with their corresponding point in the force-time plot as shown in Figure 4-1.

4.2 Acquisition of volumetric data and decomposition of data fields

The 2D displacement and strain fields obtained by DIC were stacked upon each other to create a spatio-temporal volume of data that could be decomposed using volume decomposition. Total image acquisition time during the tests was 30 ms. Analysis of the out-of-plane displacement fields revealed that the impact-induced damage developed during a period of only 6 ms of the total DIC measurement period, hence 120 DIC images were used to create the volume of data. Two types of data fields, namely out-of-plane displacement ($\boldsymbol{d_z}$) and in-plane strain in the x-direction ($\boldsymbol{\varepsilon_{xx}}$) were selected for volume decomposition. Figure 4-2 shows two sample DIC images related to ($\boldsymbol{d_z}$) and ($\boldsymbol{\varepsilon_{xx}}$) full-field measurements at maximum impact force. The presence of high strain in the middle of the sample indicated the creation of delaminations due to the impact.

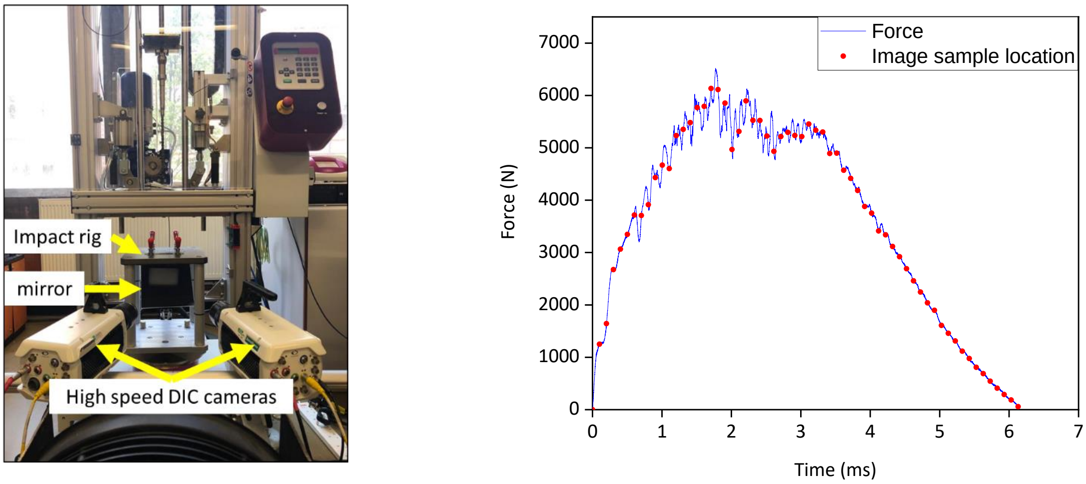

Figure 4-1 Impact test set up with a mirror beneath to capture full-field displacements using high speed DIC (left image), force-time diagram of the impact test with the time of image acquisitions indicated as red data points.

Volume decomposition was initially performed using a thousand coefficients. However, only a small number of significant coefficients were needed to represent the major characteristics of the volume. These significant coefficients have the highest absolute values in the feature vectors. The volume data can be reconstructed by using only these significant coefficients while insignificant coefficients in the feature vectors can be set to zero. The reconstructed volumes had a representation error (u_{rms}) that was calculated using the root mean square error between the actual data and its representation. To find the appropriate number of significant coefficients, one must make sure that the value of u_{rms} is less than or equal to the measurement uncertainty (u_{cal}) of the experiment [22]. Hence, the minimum number of significant coefficients required to reconstruct the volumes of DIC data in this study could be determined at the point where $u_{rms} \approx u_{cal}$. According to a previous study, the relative uncertainty (u_{rel}) associated with out-of-plane displacements obtained using the high speed DIC system used in the current project was found to be 2.4% [23]. Thus, the u_{cal} of the impact tests for the current project was calculated by multiplying the relative uncertainty by the range of the obtained measurand during the tests. u_{rms} was calculated for different numbers of significant coefficients ranging from 1 to 1000, and compared to u_{cal}. Figure 4-3 shows the plot of this comparison for different numbers of significant coefficients used to decompose d_z volumes for the two impact samples. The dashed line in the figure shows the threshold wherein $u_{rms} \approx u_{cal}$, and its intersection with the curves indicates the minimum number of significant coefficients required to accurately represent each volume of data. The plot indicates that only 77 and 61 significant coefficients out of a total of 1000 were required to reconstruct d_z volumetric data for impact sample 1 and 2, respectively. Since using 77 significant coefficients achieves the uncertainty criteria for both datasets, all d_z volumes were decomposed with this number of significant coefficients. A similar result was found for ε_{xx} volumes, wherein using 77 significant coefficients for volume decomposition ensured that the representation error was below the measurement uncertainty of the test.

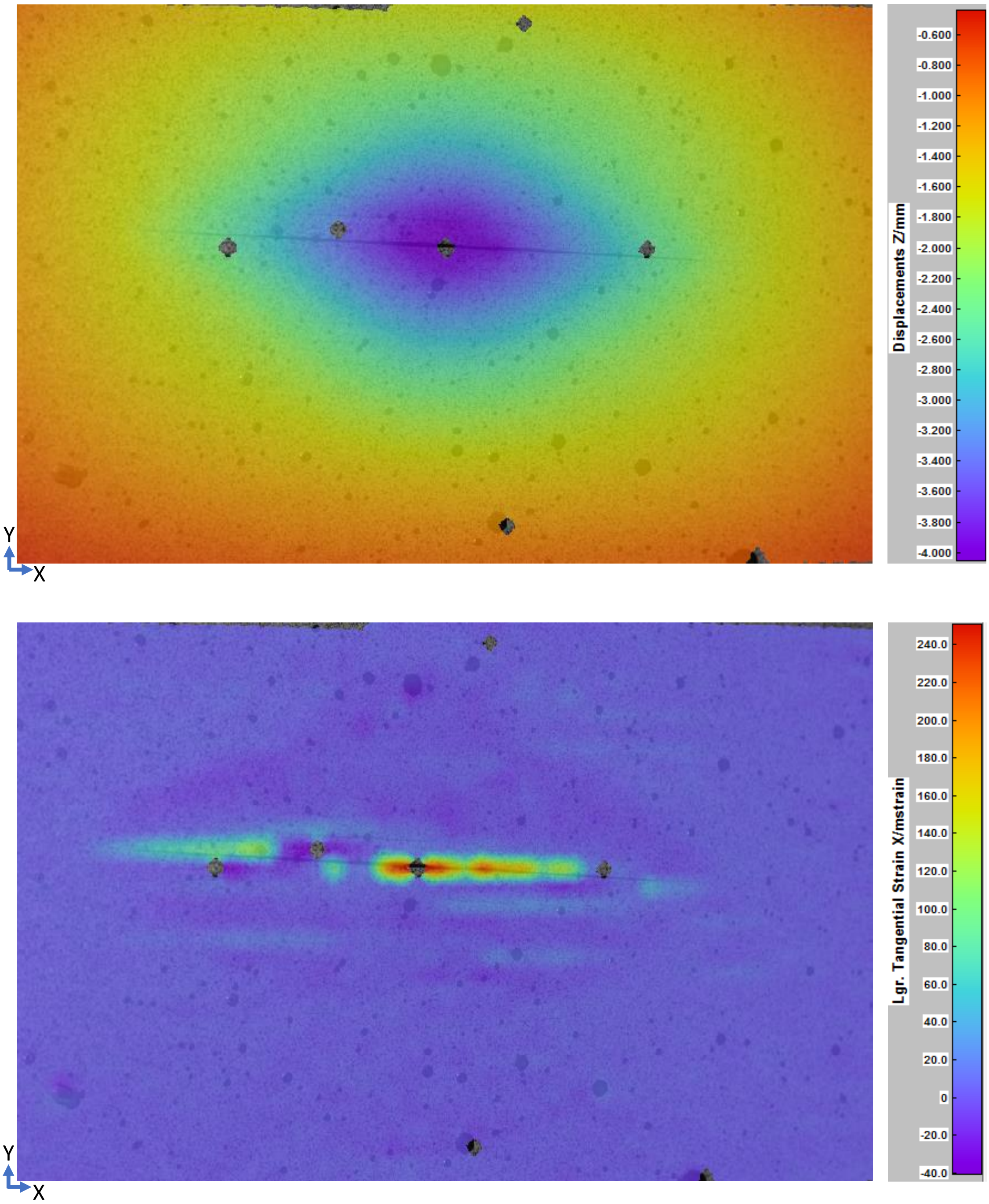

Figure 4-2 Out of plane displacement map at maximum load level (top), X-direction in-plane strain map at maximum load level (bottom). Region shown measures approximately 75 x 125 mm.

4.3 Comparison of coefficients for two impact tests

Following the orthogonal decomposition of the volumetric data from the impacts, the significant non-zero coefficients common to both volumes were plotted against one another. The two experimental data fields were compared using a method similar to that recommended in CEN-CWA 16799 Guide for Validation of Computational Solid Mechanics Models [22]. It is proposed that the two impact events can be considered to be similar if all pairs of significant coefficients fall within a band of $\pm 2\boldsymbol{u}_{exp}$ where $\boldsymbol{u}_{exp}$ is the uncertainty in the feature vectors relating to the experiment. On the other hand, two impact induced damage morphologies can be said to be different if any pair of the coefficients are out of this specified range. The uncertainty in the feature vectors was calculated as:

$$u_{exp} = \sqrt{u_{cal}^2 + u_{rms}^2} \qquad \text{Eq.3-1}$$

Figure 4-4 (top left) shows a comparison of the significant coefficients for the feature vectors describing the ***d_z*** displacement data fields during the two impact tests. All of the significant coefficients fell within the uncertainty zone indicated by the parallel red lines, suggesting that the two CFRP laminates had a similar behaviour during the impact tests in terms of out-of-plane displacements. However, when comparing coefficients for volumes associated with the ***ε_{xx}*** data fields, Figure 4-4 (top right), several coefficients were found to be outside of the uncertainty zone defined by equation 3-1. The number representing the position of the coefficients in the feature vector that result in data points outside of the uncertainty zone are given in the same figure. Among these outlier data points, two coefficients were among the first ten coefficients in the feature vector; these were coefficients number 3 and 5. Their related kernels were compared with ultrasonic pulse-echo C-scans of the impact damage. This selection was based on the fact that the first ten coefficients represent coarse characteristics of shape, such as overall orientation, and spatial density.

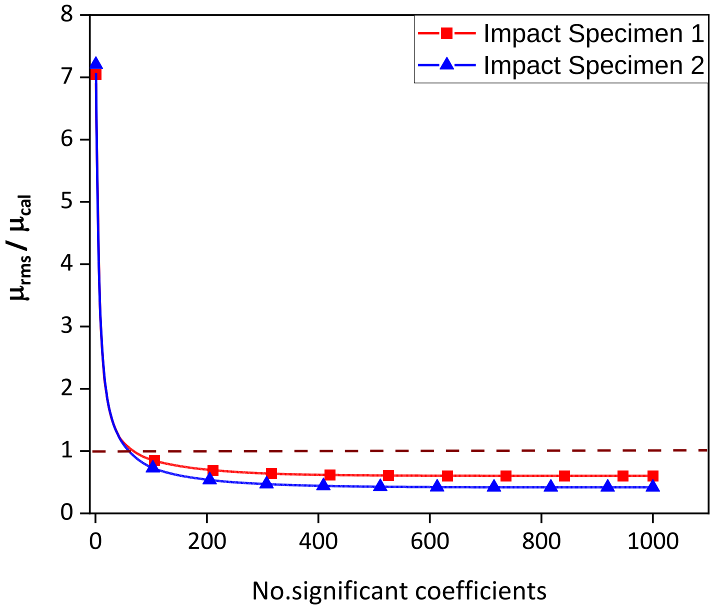

Figure 4-3 Plot showing the decrease in the ratio of representation error to measurement uncertainty, with increasing number of significant coefficients for out of plane displacement data for the two impact tests, dashed lines indicate the limit for the minimum number of required significant coefficients.

Comparisons of the damage shapes using the C-scans in Figure 4-4 (bottom) indicate that the impact damage in the first specimen was smaller than that in the second specimen. The C-scan of the second specimen showed a significant delamination on the left side of the sample which differentiated it from the damage morphology of first impact test. This asymmetric damage morphology corresponds with the asymmetric shape represented by the third kernel shown in Figure 4-5 (left). The length of the impact damage in the X-direction is larger for the second specimen. This difference in size is related to the shape represented by the fifth kernel as seen in Figure 4-5 (right). Based on these initial observations, comparisons of feature vectors representing the spatio-temporal variations in deformation during impact events can help to understand the causes of the differences in the resulting damage morphologies.

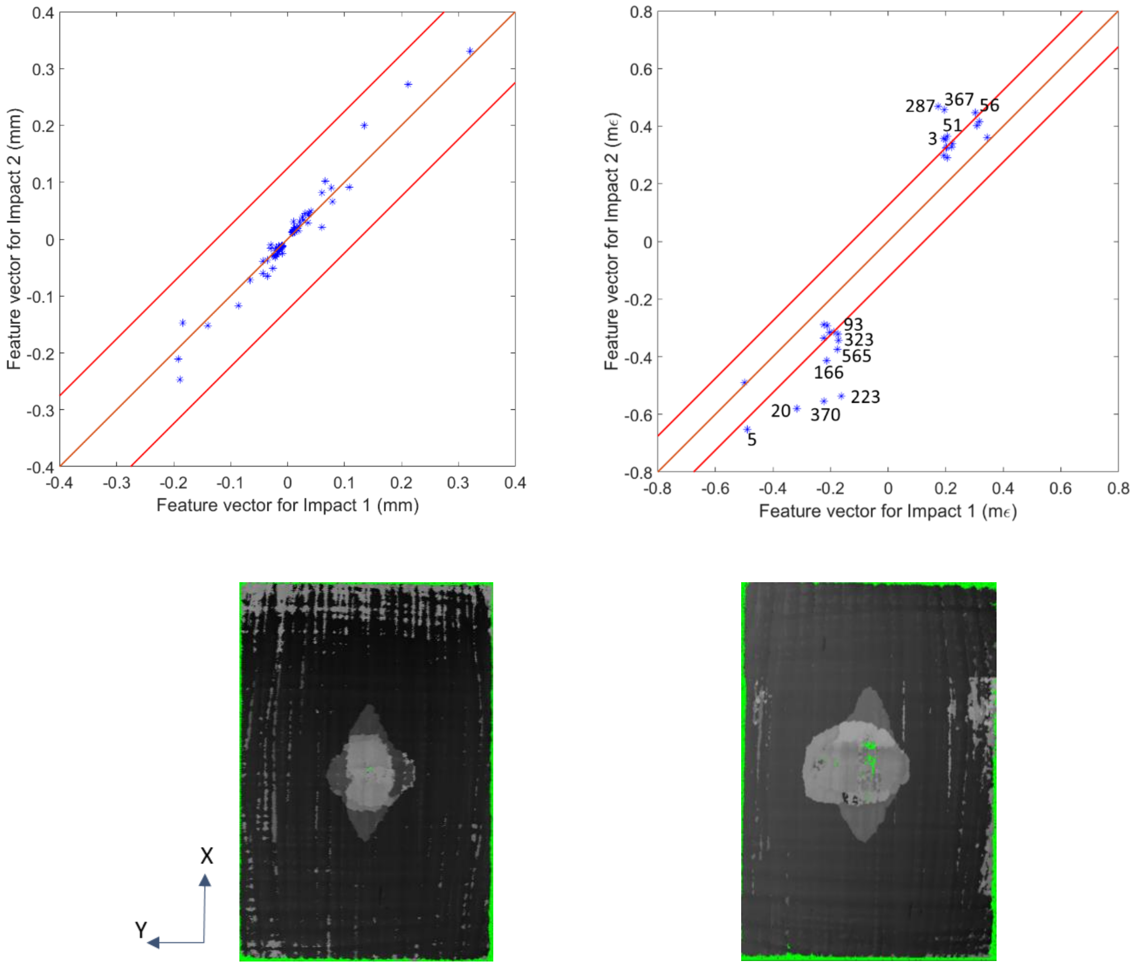

Figure 4-4 Comparison of feature vectors for out of plane data fields of two impact tests (top left), comparison of feature vectors for X-direction in-plane strain fields of two impact tests (top right), C-scan of impact damage area for impact sample 1 (bottom left), and impact sample 2 (bottom right).

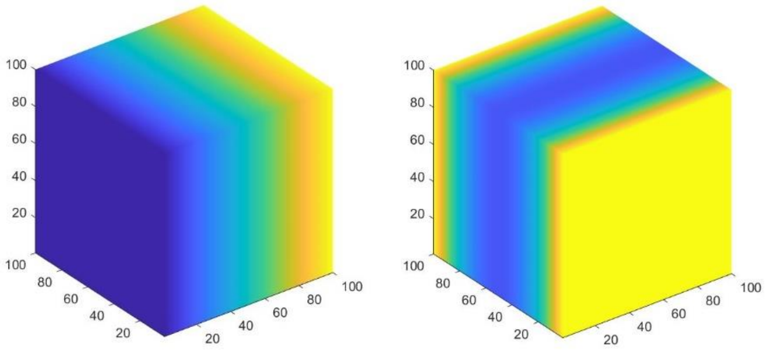

Kernel 3

Kernel 5

Figure 4-5 Kernels associated with largest absolute valued coefficients outside of the uncertainty zone defined by equation 3-1. Kernel 3 represents the difference in symmetry along the y-axis between the two impacts in Figure 4-4, and Kernel 5 the difference in length in the x direction.

4.4 Fatigue tests

Decomposition has also been used to explore how damage in composites grows during fatigue tests. Laminates were manufactured using the same procedure described in Section 4.1, however a $[45/-45]_{3s}$ layup was used as it is known from prior experiments to have a more progressive failure in fatigue than laminates with a $[0_2/90_2]_{2s}$ layup. The laminates were then cut into 40 mm by 200 mm coupons. A horizontal slot was milled into the centre of the coupons using a silicon carbide milling bit. This slot acted as a stress raiser such that fatigue damage would coalesce around it during the tests.

The specimens were loaded in tension-tension fatigue using an Instron 8501 universal testing machine (Instron, Norwood MA, USA) running at 19 Hz using a maximum load of 7.75 kN and minimum load of 0.78 kN. The slotted area of the specimen was monitored using a DeltaTherm 1780 system (Stress Photonics, Madison WI, USA). The DeltaTherm system yielded full-field data representing the distribution of stress on the surface of the specimen by monitoring the thermoelastic emissions caused by the cyclical stresses [24]. Full-field data were captured with a 6 s time period between sequential fields. The progression of fatigue damage can be seen in Figure 4-6. The first image on the left shows the stress-concentration around the slot at the start of the test, which steadily changed over time as matrix cracking and delaminations formed in the specimen.

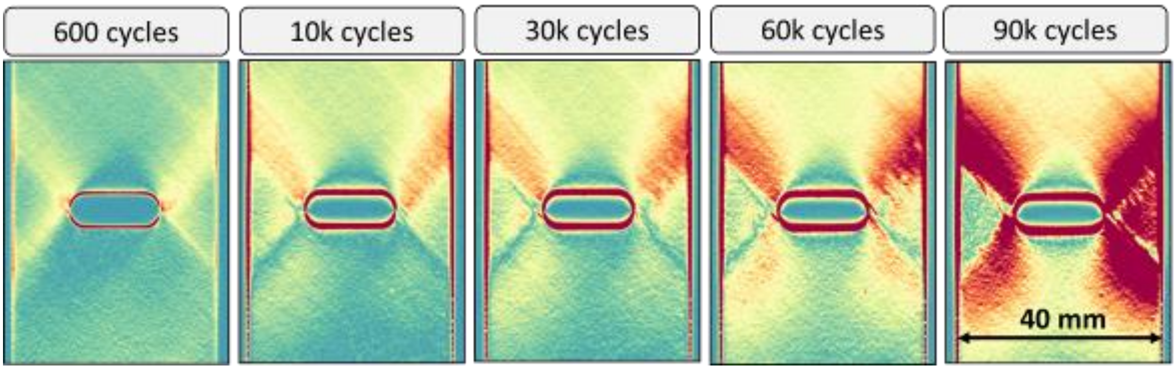

Figure 4-6 Full-field thermoelastic data for a fatigued specimen at given number of load cycles.

In order to automate the processing of fatigue data, an algorithm was written to process the full-field thermoelastic data based on a previously developed technique used for processing DIC data [15]. Firstly, each data field was decomposed into a feature vector using 2D orthogonal decomposition. Subsequently the amount of change between sequential fields was quantified by calculating the difference between their corresponding feature vectors. By monitoring feature vector difference it was possible to automatically identify intervals of the test when damage propagated rapidly. The spatial distribution of damage that developed during the identified intervals was determined by subtracting the full-field data at the start of the interval from the data at the end, this resulted in a difference map where high levels of difference corresponded with the locations in which damage was propagating. These high difference areas were determined using adaptive thresholding, resulting in a binary image showing where damage propagated during the interval. The binary images for each interval of damage propagation were then overlaid, with the colour for each image set to indicate the cycle at which the interval occurred during the test. This resulted in a damage-cycle map, shown in Figure 4-7 left.

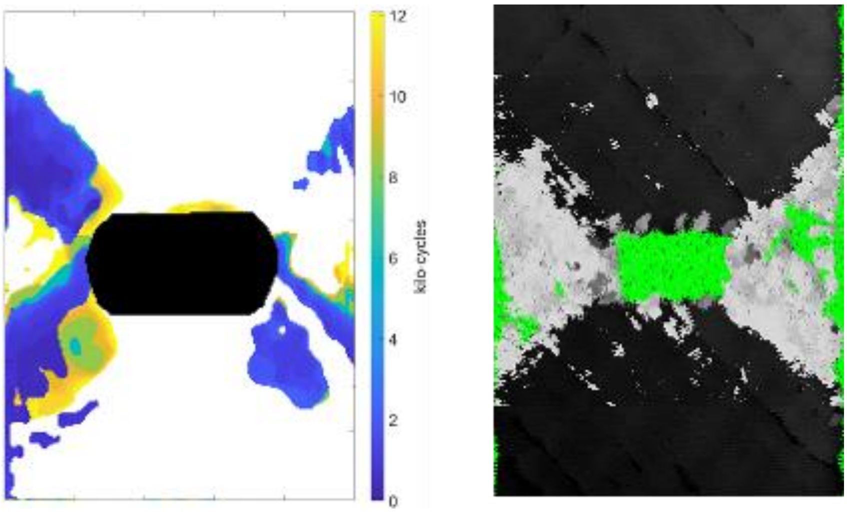

Figure 4-7 A damage-cycle map for a fatigues composite specimen (left), and an ultrasonic C-scan of the specimen post test showing damaged locations (specimen width 40 mm).

The damage-cycle maps were qualitatively compared with ultrasonic C-scans of the same specimens and the morphology of the damage according to the two techniques found to be similar (e.g., Figure 4-7). The benefit of capturing damage-cycle maps compared to ultrasonic inspection is that the fatigue test does not need to be interrupted in order to determine the morphology of damage. Thus, damage at any stage of the test can be determined resulting in greater insight into the fatigue process of composite materials.

5. Conclusions

A method has been developed to segment MRZs in 3D serial-section datasets of composite materials by using simple image processing techniques. The 3D shape of microstructural objects has been decomposed using the volume decomposition technique to characterise the main shape features of each individual object. It was shown that MRZs possess a complex morphology when compared to voids, and their relative shape can signify their location within the fibre weave. It was also shown that applying volume decomposition to objects consisting of millions of voxels can reduce the data to a few hundred significant coefficients with a representation error of less than one voxel. The relationship between the kernels associated with significant coefficients in a feature vector and major shape characteristics of a microstructural object has been demonstrated. Thus, feature vectors can be used to compare the morphology of microstructural objects and possibly quantify their relationships. The similarity of MRZs has been calculated by comparison between feature vectors. From these feature vector comparisons, MRZs can be sorted into three clusters representing interlaminar, intralaminar and tow cross MRZs.

Volume decomposition has been used to identify damage locations in tomography data at two different length scales: individual fibres and within the bulk volume. Indications of damage are given by high difference between the feature vectors, which correlate to visually observable damage at both length scales. Detailed analysis of individual fibres using 2D orthogonal decomposition leads to the possibility of correlating regions of damage to microstructural features, such as fibre twist.

Volumes of deformation data obtained using a high-speed DIC system were decomposed using volume decomposition. The volumetric data for each impact test was represented using a feature vector and the significant coefficients of that vector were compared with those of the other impact test. Using a similar approach as that described in CEN-CWA 16799, the feature vectors were compared and the differences linked to the resultant damage morphology. Results reveal that outlier coefficients in the comparison plots could be linked to the differences between the morphology of impact damage. Work has also demonstrated that the propagation of damage during a dynamic test can be extracted from full-field data using 2D orthogonal decomposition. An algorithm has been developed for obtaining damage-cycle maps that show how fatigue damage grows within composite specimens.

There are several avenues for future work from the work carried out in this project. These decomposition techniques have the potential to be used for a range of applications in further research. For example, the decomposition techniques utilised in this research have potential application at the macroscale to explore the damage and failure response of ceramic structural panels subject to the coupled interaction of humidity, thermal state and dynamic loading experience during persistent operations of hypersonic aircraft.

These techniques can also be used to advance the comparison of microscale experimental and simulation data such that models of composite behaviour and damage propagation can be quantitatively validated.

The fibre tracking algorithm developed in this work can be applied to other materials. The combination of three-dimensional and two-dimensional orthogonal decomposition of datasets can be explored further, to determine if this approach can indicate correlations between specimen structure and damage location.

This project has successfully applied data decomposition techniques to a range of datasets, across three objectives, to quantify microstructural features and damage locations. Significant outputs are planned to be presented as one conference presentation, and two peer-reviewed articles. The results of this work also lead to suggestions for further applications of 2D and 3D orthogonal decomposition approaches.

References

1. Alexiadis, A., S. Ferson, and E.A. Patterson, *Transformation of measurement uncertainties into low-dimensional feature vector space.* Royal Society Open Science, 2021. **8**(3): p. 201086.
2. Ohnabe, H., S. Masaki, M. Onozuka, K. Miyahara, and T. Sasa, *Potential application of ceramic matrix composites to aero-engine components.* Composites Part A: Applied Science and Manufacturing, 1999. **30**(4): p. 489-496.
3. Okita, Y., Y. Mizokami, and J. Hasegawa, *Experimental and Numerical Investigation of Environmental Barrier Coated Ceramic Matrix Composite Turbine Airfoil Erosion.* Journal of Engineering for Gas Turbines and Power, 2018. **141**(3).
4. Walock, M.J., V. Heng, A. Nieto, A. Ghoshal, M. Murugan, and D. Driemeyer, *Ceramic Matrix Composite Materials for Engine Exhaust Systems on Next-Generation Vertical Lift Vehicles.* Journal of Engineering for Gas Turbines and Power, 2018. **140**(10).
5. Binner, J., M. Porter, B. Baker, J. Zou, V. Venkatachalam, V.R. Diaz, A. D'Angio, P. Ramanujam, T. Zhang, and T.S.R.C. Murthy, *Selection, processing, properties and applications of ultra-high temperature ceramic matrix composites, UHTCMCs – a review.* International Materials Reviews, 2020. **65**(7): p. 389-444.
6. Estili, M. and Y. Sakka, *Recent advances in understanding the reinforcing ability and mechanism of carbon nanotubes in ceramic matrix composites.* Science and Technology of Advanced Materials, 2014. **15**(6): p. 064902.

7. Khan, R.M.A., B.A. Ahmed, M.M. Al Malki, A.S. Hakeem, and T. Laoui, *Synthesis of hard and tough calcium stabilized α-sialon/SiC ceramic composites using nano-sized precursors and spark plasma sintering.* Journal of Alloys and Compounds, 2018. **757**: p. 200-208.
8. Lv, X., F. Ye, L. Cheng, and L. Zhang, *Novel processing strategy and challenges on whisker-reinforced ceramic matrix composites.* Composites Part A: Applied Science and Manufacturing, 2022. **158**: p. 106974.
9. Morales-Rodríguez, A., P. Reynaud, G. Fantozzi, J. Adrien, and E. Maire, *Porosity analysis of long-fiber-reinforced ceramic matrix composites using X-ray tomography.* Scripta Materialia, 2009. **60**(6): p. 388-390.
10. Santhosh, U., Y. Gowayed, G. Ojard, I. Smyth, S. Kalarikkal, and G. Jefferson, *Quantification of Porosity in Ceramic Matrix Composites Using Thermography.* Journal of Nondestructive Evaluation, 2018. **37**(2): p. 37.
11. Yang, S., A. Tewari, and A.M. Gokhale, *MODELING OF NON-UNIFORM SPATIAL ARRANGEMENT OF FIBERS IN A CERAMIC MATRIX COMPOSITE.* Acta Materialia, 1997. **45**(7): p. 3059-3069.
12. Christian, W.J.R., K. Dvurecenska, K. Amjad, C. Przybyla, and E.A. Patterson, *Machine vision characterisation of the 3D microstructure of ceramic matrix composites.* Journal of Composite Materials, 2019. **53**(16): p. 2285-2296.
13. Middleton, C., M. Weihrauch, W. Christian, R. Greene, and E. Patterson, *Detection and tracking of cracks based on thermoelastic stress analysis.* Royal Society open science, 2020. **7**(12): p. 200823.
14. Amjad, K., W. Christian, K. Dvurecenska, D. Mollenhauer, C. Przybyla, and E. Patterson, *Quantitative comparisons of volumetric datasets from experiments and computational models.* Royal Society open science, 2022.
15. Christian, W., K. Dvurecenska, K. Amjad, J. Pierce, C. Przybyla, and E. Patterson, *Real-time quantification of damage in structural materials during mechanical testing.* Royal Society open science, 2020. **7**(3): p. 191407.
16. Zitova, B. and J. Flusser, *Image registration methods: a survey.* Image and vision computing, 2003. **21**(11): p. 977-1000.
17. Gowayed, Y., G. Ojard, E. Prevost, U. Santhosh, and G. Jefferson, *Defects in ceramic matrix composites and their impact on elastic properties.* Composites Part B: Engineering, 2013. **55**: p. 167-175.
18. Creveling, P.J., J. Fisher, N. LeBaron, and M.W. Czabaj, *4D Imaging of ceramic matrix composites during polymer infiltration and pyrolysis.* Acta Materialia, 2020. **201**: p. 547-560.
19. Dvurecenska, K., I. Diamantakos, E. Hack, G. Lampeas, E.A. Patterson, and T. Siebert, *The validation of a full-field deformation analysis of an aircraft panel: A case study.* The Journal of Strain Analysis for Engineering Design, 2021. **56**(4): p. 265-272.
20. Lampeas, G., V. Pasialis, X. Lin, and E. Patterson, *On the validation of solid mechanics models using optical measurements and data decomposition.* Simulation Modelling Practice and Theory, 2015. **52**: p. 92-107.
21. Jones, E.M.C. and M.A. Iadicola, *A Good Practices Guide for Digital Image Correlation*. 2018, International Digital Image Correlation Society.
22. de Normalization, C.E., *Validation of computational solid mechanics models.* CWA, 2014. **16799**: p. 2014.
23. Hack, E., X. Lin, E. Patterson, and C. Sebastian, *A reference material for establishing uncertainties in full-field displacement measurements.* Measurement Science and Technology, 2015. **26**(7): p. 075004.
24. Greene, R.J., Patterson, E.A., Rowlands, R.E. (2008). Thermoelastic Stress Analysis. In: Sharpe, W. (eds) Springer Handbook of Experimental Solid Mechanics. Springer Handbooks. Springer, Boston, MA.